Submitted: 22.03.2023.
Accepted for publication: 10.04.2023.

Characterization of Cobalt Ferrite Nanoparticles Obtained by Various Synthesis Methods and Comparison with the Raman Spectra of Other Ferrites and Some Cubic Oxide Spinels

https://doi.org/10.2298/SOS230322035L

Zorica Ž. Lazarević[1,*], Aleksandra Milutinović[1], Ljubica Andjelković[2], Milica Petrović[1], Branka Hadžić[1], Maja Romčević[1], Jelena Trajić[1], Nebojša Ž. Romčević[1]

[1]*Institute of Physics, University of Belgrade, Pregrevica 118, Zemun, Belgrade, Serbia*
[2]*University of Belgrade, Institute of Chemistry, Technology and Metallurgy, Department of Chemistry, 11000 Belgrade, Serbia*

Abstract

Single phase cobalt ferrite ($CoFe_2O_4$) with nanoparticles of similar sizes (15.7-19 nm) was obtained by different synthesis methods: coprecipitation, ultrasonically assisted coprecipitation, coprecipitation followed by mechanochemical treatment, microemulsion and microwave assisted hydrothermal synthesis. The obtained $CoFe_2O_4$ samples have been studied using a variety of characterization techniques: X-ray diffraction (XRD), Raman spectroscopy, far infrared (FIR) reflectivity and attenuated total reflectance (ATR) in combination with Fourier-transform infrared (FTIR) spectroscopy in mid IR spectra. Different methods of synthesis produced nanoparticles with different lattice constants, internal stresses and different cation inversion values. This is confirmed in the subtle changes in the Raman and IR spectra of different $CoFe_2O_4$ nano-powders. The Raman spectra of $CoFe_2O_4$ were compared with the spectra of other ferrites and some cubic oxide spinels in an attempt to evaluate the contribution of tetrahedral and octahedral oscillations in certain Raman modes.

Keywords: *$CoFe_2O_4$, Nanoparticles, Raman spectroscopy, FIR reflectivity, ATR-FTIR spectroscopy.*

Карактеризација наночестица кобалт ферита добијених различитим методама синтезе и поређење са Рамановим спектрима других ферита и неких кубичних оксидних спинела

Садржај: Монофазни кобалт ферит са наночестицама сличних величина (15,7-19 нанометара) добијен је различитим методама синтезе: копреципитацијом, ултразвучно потпомогнутом копреципитацијом, копреципитацијом праћеном механохемијском синтезом, микроемулзијом и микроталасном хидротермалном синтезом. Добијени узорци кобалт ферита су проучавани коришћењем различитих техника карактеризације: дифракцијом рендгенских зрака на праху, Раман спектроскопијом, рефлексијом у далекој инфра-црвеној области (ИЦ) и методом апсорпције при вишеструкој тоталној рефлексији у комбинацији са инфра-црвеном спектроскопијом (АТР-ИЦ) у средњој инфра црвеној области. Различитим методама синтезе добијене су наночестице са различитим константама решетке, унутрашњим напрезањима и различитим вредностима инверзије катјона. Ово је потврђено у суптилним променама у Раман и ИЦ спектрима различитих нано-прахова кобалт ферита. Раман спектри кобалт ферита упоређени су са спектрима других ферита и неких кубних оксидних спинела у покушају да се процени утицај удела тетраедарских и октаедарских осцилација у одређеним Раман модовима.

Кључне речи: *$CoFe_2O_4$, Наночестице, Раман спектроскопија, Рефлексија у далекој инфра црвеној области, АТР-ИЦ спектроскопија.*

Characterization of Cobalt Ferrite Nanoparticles Obtained by Various Synthesis Methods and Comparison with the Raman Spectra of Other Ferrites and Some Cubic Oxide Spinels

Zorica Ž. Lazarević[1,*], Aleksandra Milutinović[1], Ljubica Andjelković[2], Milica Petrović[1], Branka Hadžić[1], Maja Romčević[1], Jelena Trajić[1], Nebojša Ž. Romčević[1]

[*]**corresponding author**:

Zorica Ž. Lazarević

Pregrevica 118,

Belgrade, Serbia

Fax: +381 11 31 61 536

Phone: +381 11 37 13 035

Email: **lzorica@yahoo.com**

1. Introduction

Ferrite materials have long been known in the literature. It is notable that in recent decades, spinel ferrite nanomaterials have attracted great interest in various fields of nanoscience and technology owing to their exceptional characteristics at nanometric sizes [1-3]. Spinel ferrites are the topic of numerous studies due to their magnetic nature and crystalline structure. Small changes of the particle size, composition or presence of surface effects give them unique magnetic features. Nanosized spinel ferrites received a huge amount of interest due to their low cost, excellent chemical stability, moderate saturation magnetization, high surface area, high wear resistance, low density, low thermal expansion coefficient, and low toxicity to both human health and environment. They have application in diverse fields such as high density information storage systems, magnetic cores, catalysts, electronic devices, ferrofluids, humidity sensors, magnetic drug delivery, antenna material and microwave absorbers [4]. It is well known that properties of ferrite materials strongly depend on the preparation conditions. One of the most interesting ferrites is cobalt ferrite ($CoFe_2O_4$).

Cobalt ferrite ($CoFe_2O_4$) is a ferrimagnetic material characterized by a high Curie temperature at T = 793K. The $CoFe_2O_4$ has an inverse spinel structure with oxygen atoms at the FCC lattice and one half of Fe^{3+} ions occupying the tetrahedral A sites while the other half together with Co^{2+} occupy the octahedral B site [5]. Technological and scientific challenges coupled with environmental considerations have prompted a search for simple and energy-efficient synthesis and processing routes of nanocrystalline spinel ferrites. Among the many types of preparation and processing techniques including, for example, hydrothermal reactions, coprecipitation, sol-gel method, microwave and mechanochemical route has been recognized as a powerful method for the production of novel, high-performance, and low-cost materials [6-10].

In this work the cobalt ferrite ($CoFe_2O_4$) nanoparticles are synthesized using five different methods (US-CO ultrasonically assisted coprecipitation, CO - coprecipitation, MC-CO coprecipitation followed by mechanochemical treatment, MW-HT microwave assisted hydrothermal method and ME microemulsion method) [10]. All as-prepared nano-powders were sintered at 400ºC for two hours. The influence of different synthesis methods on the spectroscopic and vibrational characteristics of the obtained samples was investigated. In the

literature, there are large discrepancies in assumptions about the origin and type of oscillations in the Raman and IR spectra of ferrites. The Raman spectra of $CoFe_2O_4$ were compared with the spectra of other ferrites and some cubic oxide spinels in an attempt to evaluate the contribution of tetrahedral and octahedral oscillations in certain Raman modes.

2. Experimental procedure

XRD patterns were collected using a Rigaku SmartLab automated powder X-ray diffractometer with Cu Kα1 (λ = 1.54059 Å) radiation. The diffraction range was 15-90º with a step of 0.01º at a scan speed of 2º min^{-1}.

The Raman spectra were taken in the backscattering configuration by Jobin Yvon T64000 spectrometer, equipped with nitrogen cooled charged coupled device detector. As an excitation source we used the 532 nm line of Ti:Sapphire laser, with laser power 20 mW. The measurements were performed in the spectrum range 100- 1000 cm^{-1}.

The FIR reflectivity measurements were carried out with a BOMEM DA-8 FIR spectrometer. A deuterated triglycine sulphate (DTGS) pyroelectric detector was used to cover the wave number range from 70-700 cm^{-1}.

ATR-FTIR spectra of $CoFe_2O_4$ nanoparticle samples were recorded in the mid-infrared (MIR) region from 400 to 4000 cm^{-1}.

3. Results and discussions

3.1. XRD

X-ray diffractograms of cobalt ferrite nanoparticle samples obtained by various synthesis methods are presented in Fig.1a). All implemented methods give well crystalized single-phase samples with cubic spinel structure ($Fd\bar{3}m$ space group) and characteristic Bragg reflections. Diffractograms are analyzed by *FullProf Suite* [11]. Lattice constants (a) and average size of nanoparticles (D) obtained by Rietveld refinement are given with corresponding diffractograms. In Fig.1b) are extracted dominant (311) Bragg reflections and can be easily seen the shift of these reflections towards low 2θ angles with an increase in the lattice constant of the nanoparticles. It can also be seen that sample “ME” obtained by microemulsion method, has slightly larger nanoparticles than the other samples.

Figure 1

Fig. 1c) shows dependence of the degree of the cation inversion (x) in cobalt ferrite nanoparticles on the lattice constant. Triangles are values obtained by Rietveld refinement and circles are values obtained by the structural analysis.

XRD analysis shows that different synthesis methods yielded $CoFe_2O_4$ nanoparticles of similar average sizes (which was our intention) with cation inversion (x) in a fairly wide interval: from 0.59 to 0.80, according to Rietveld analysis, or 0.58 - 0.85 according to structural analysis. More on that elsewhere. Such, mostly inverse, $CoFe_2O_4$ cubic spinels can be represented by the formula $(Co_{1-x}Fe_x)^t[Fe_{2-x}Co_x]^oO_4$, where $(Co_{1-x}Fe_x)^t$ is a tetrahedral complex (A) and $[Fe_{2-x}Co_x]^o$ octahedral one ($[B_2]$). Different cations in tetrahedral and also in octahedral sites change the crystal symmetry both in relation to the pure normal spinel structure (x=0) and in relation to the completely inverse structure (x=1), but the X-diffractometry of the nanoparticles shows an averaged symmetry that does not differ from the symmetry of normal cubic spinels.

3.2. Crystal lattice dynamics of cubic spinels - an overview

The full unit cell of normal cubic spinel, $(A)^t[B_2]^oX_4$, with the space group $Fd\bar{3}m$ (No. 227), contains 56 atoms, i.e. Z = 8 formula units. The smallest symmetry unit is the rhombohedral primitive Bravais cell that contains 14 atoms (two formula units). The complete vibrational spectrum can be classified in terms of the vibrations of a single primitive cell. Each normal mode of the unit cell corresponds to N normal modes of the crystal which differ principally in the phase shift between adjacent cells. Factor group analysis predicts $3 \cdot 14 = 42$ phonon modes: 3 acoustic modes of F_{1u} symmetry and 39 optic modes that are distributed among the following symmetries at the Brillouin zone centre [12, 13]:

$$\Gamma = A_{1g}(\mathrm{R}) + E_g(\mathrm{R}) + 3F_{2g}(\mathrm{R}) + 4F_{1u}(\mathrm{IR}) + F_{1g}(\mathrm{in}) + 2A_{2u}(\mathrm{in}) + 2E_u(\mathrm{in}) + 2F_{2u}(\mathrm{in}) \qquad (1)$$

Five of these phonon modes are Raman active, namely A_{1g}, E_g and $3F_{2g}$; four are IR active, $4F_{1u}$, and remaining modes are silent (inactive). (A-modes are singlets, E-doublets and F-modes are triplets.)

The symmetries and selection rules for the normal modes of spinel-type cubic compounds yields phonons which originate from following atomic displacement [12, 14-16]:

$$\Gamma_{(A)8a} = F_{2g}(\mathrm{R}) + F_{1u}(\mathrm{IR});$$

$$\Gamma_{(B)16d} = 2F_{1u}(\mathrm{IR}) + A_{2u}(\mathrm{in}) + E_u(\mathrm{in}) + F_{2u}(\mathrm{in});$$

$$\Gamma_{(O)32e} = A_{1g}(\mathrm{R}) + E_g(\mathrm{R}) + F_{1g}(\mathrm{in}) + 2F_{2g}(\mathrm{R}) + A_{2u}(\mathrm{in}) + E_u(\mathrm{in}) + 2F_{1u}(\mathrm{IR}) + F_{2u}(\mathrm{in}) \qquad (2)$$

As can be seen, octahedral cations do not move in Raman modes, they are mostly anions that participate in all modes, while A - cations contribute in F_{2g} Raman modes. Group theory for all IR modes predicts the displacement of both A- and B-cations. It is considered that in two strong modes at higher wave numbers this movement is negligible - that mainly anions oscillate, while in two weak F_{1u} modes the movement of cations becomes significant.

A-site tetrahedra in spinel are isolated from each other and share corners with neighbouring B-site octahedra. No edge sharing occurs between A-site tetrahedra and other A- or B-site polyhedra. On the other side, B-site octahedra share six of twelve O-O edges with nearest-neighbour B-site octahedra forming "lattice of condensed octahedra", to cite Preudhomme at al. [17, 18]. However, some anion vibrations may be more affected by tetrahedral cations than octahedral cations and vice versa.

There are various interactions between ions, such as short-range valence forces (bonding and repulsive), induced polarizability Coulomb interactions (in the rigid–ion approximation only Coulomb static forces are considered) and exchange interactions (often neglected) that are relevant for determining phonon energies. Lattice dynamical calculations have been performed for some cubic spinels using the different theoretical models [12, 19]. Raman data of single crystal, as well as the IR transversal and longitudinal optical zone centre phonon frequencies, are necessary to reliably determine the input parameters for a calculation in which at least 6 force constants for bonding and repulsive forces, dynamic charges, and polarizabilities are treated as variables. The force constants were fitted in such a manner so as to achieve an overall good agreement with the available zone-centre Raman and infrared experimental results. (Other input parameters are the fractional coordinates (x, y, z), the unit cell dimensions *a*, the structural parameters *u*, the masses of the atoms and the symmetry coordinates for allowed modes.) A large number of physical quantities that are fitted can lead to erroneous results (*i.e.* values that have no physical sense). Therefore, simpler models are preferred as "first attempt" – like short range model (SRM), rigid ion model (RIM) and at the end - polarizable ion model (PIM). In the middle of the last century the lack of reliable experimental data and low computer capacity were the reasons for introducing various approximations in lattice dynamical calculations and force constants fitting.

The first comprehensive study of infrared spectra of ferrite spinels $M\mathrm{Fe_2O_4}$ (M^{2+} = Co, Fe, Mg, Mn, Ni, Zn) was done by Waldron in 1955 [20]. Theoretical interpretation of spectra was given with some approximations. Since there were only two IR modes in the measured range of the ferrite IR spectrum (meaning that only two force constants can be calculated), he had to simplify the potential energy model. As bending forces are remarkably weaker than stretching forces (and repulsive forces, also), Waldron neglected bending forces and his expression for the

potential energy became: $2V = k_t\Sigma r_t^2 + k_o\Sigma r_o^2$. In this relation k_t, and k_o, designate the force constants associated with unit displacement of the tetrahedral and octahedral bonds, respectively, and r_t and r_o, represent the corresponding components of displacement from equilibrium in the direction of the appropriate bonds. In this simplified model the lowest IR oscillation frequency ω_4 is zero. (By including the bending forces in the potential, a value of ω_4 other than zero is obtained.) Waldron made an assumption that two strong IR modes must be connected solely with oxygen anion vibrations, and the other two (which were beyond the range of his measurement) with vibrations that include cations. Thereby, mode of the highest wave number arises in tetrahedral stretching; next mode is assigned as stretching vibration of the octahedral groups, and two low modes as translations of tetrahedra and octahedra, respectively.

In later experimental and theoretical work on different types of spinels [12, 21], it was shown that Waldron approximation could be applied unreservedly, only in cases where tetrahedral bonding forces are significantly stronger than octahedral bonding forces. Tetrahedral oscillations can then be considered to be practically independent of octahedral oscillations. Generally, the stretching frequency, and the bonding force, strongly depends on the valence of the cation. In $A^{2+}B^{3+}{}_2X_4$ (II-III) normal spinels trivalent cations commonly give stronger bonding forces. Preudhomme and Tarte [21] have shown that the high-frequency band must be assigned to a vibration of the tetrahedral group when this group is occupied by the highest-valence cation of the compound, as in germanates $Me_2^{2+}GeO_4$ and some other II-IV spinels like molibdates and wanadates.

In the inverse ferrite spinels the highest-valence cation Fe^{3+} is in tetrahedral position and Waldron's model provides acceptable stretching force constants. A great number of researchers still use his formulas to calculate the force constants of spinels.

In later theoretical researches were used more precise models that monitored vibrations of all atoms in the primitive cell and their interactions [12, 19, 22, 23]. These calculation models confirmed that potential of the $(A)^t[B_2]^oX_4$ spinel structure is mainly controlled by stretching of the octahedral B-X bonds and tetrahedral A-X bonds and that repulsive forces between X-X anions and between (mostly B-B) cations can be significant, also. Bending forces are usually very weak in all spinels. It is pointed out that it is not possible to divide the modes into vibrations of isolated AO_4 or BO_6 units. Modes must be regarded as coupled vibrations of various contributions. For instance, to potential energy of A_{1g} mode of sulphide spinel $MnCr_2S_4$, according to Lutz at al. [12], predominantly contribute repulsive forces of anions (50%). Bonding forces between octahedral cation and anion, B-X (35%) and tetrahedral A-X forces (15%) have a significantly smaller contribution. In mode E_g dominate octahedral B-X bonding forces (76%). In addition, there are repulsive forces of anions and Coulomb forces. A mode

$F_{2g}(1)$ can be described as a "combination" of translation a tetrahedral AX4 (62%) and an octahedral BX6 unit (25%). IR mode $F_{1u}(4)$ has origin dominantly in stretching vibrations - more octahedral and less tetrahedral, and $F_{1u}(3)$ as a "combination" of 81% octahedral B-X, 7% tetrahedral A-X and 9% bending forces X-B-X.

In oxide spinels is relatively small contribution of O-O and B-B repulsive interactions what is reasonable because the O-O and B-B distances ($(\sqrt{2}/4)\cdot a$ = $0.353553\cdot a$) are larger compared to the respective ionic radii than in the case of sulphide spinels. (r_O = 1.38 Å, for $ZnCr_2O_4$: $R_{O\text{-}O} = R_{B\text{-}B}$ = 0.36553·8.321 =3.04 Å, $2\cdot r_O$ = 2.76 Å; r_S =1.84 Å, for $MnCr_2S_4$: $R_{S\text{-}S} = R_{B\text{-}B}$= 0.36553·9.794 Å=3.58 Å, $2\cdot r_S$=3.68 Å) [23]. Smaller unit-cell dimensions and greater ionic charges, gives rise to a higher valence force constants k_t and k_o (for $ZnCr_2O_4$ is k_t =180 N m^{-1} and k_o = 210 N m^{-1}) compared to those of spinel-type chromium sulphides (for $MnCr_2S_4$: 42 and 85 N m^{-1}). At the same time, repulsive force constants in $ZnCr_2O_4$ oxide spinels are much smaller (Cr-Cr repulsive force constant ~ 32 N/m and O-O constants < 10 N m^{-1}), only 18% to 5% of stretching force constants. According to Ref. [23], the main contribution to the potential energy of A_{1g} mode in $ZnCr_2O_4$ is given by the stretching forces between tetrahedral A-cation and anion X (40%) and octahedral B-X forces (35%). Repulsive O-O forces contribution is only 8%. In mode E_g dominate octahedral B-X stretching forces, as in chromium sulphides. In other modes contribution of repulsive O-O forces is even lower, 2 - 4%. Exception is $F_{1u}(1)$ IR mode where A-X is about 30%, B-X 15% and repulsive Cr-Cr force 17%. Bending forces participate only in few silent modes. In Ref. [19] were obtained lower values for stretching forces and higher for oxygen repulsion. The calculation yielded low values of bending forces (max 3.75 N m^{-1}), but unfortunately it were not given the potential energy distributions of phonons.

It is clear from these examples that the modes of a particular spinel can be assigned only on the basis of theoretical calculations of crystal lattice dynamics with input of relevant experimental data obtained from IR and Raman spectra recorded on crystal samples.

Cation redistribution over the tetrahedral and octahedral sites alters the local symmetry and form partially inverse and inverse spinel structure. Ferrite spinels $(M_{1-x}Fe_x)^t[Fe_{2-x}M_x]^oO_4$ are typical inverse spinels, except $ZnFe_2O_4$. Antonov and Harmon [24] show that in a frame of cubic symmetry, by density functional theory calculations (LSDA+U), all macroscopic magnetic and insulating properties for Co-, Ni-, and Mn-ferrites (inverse spinels) can be correctly described. However, the Raman spectra of inverse and partially inverse spinel ferrites have more peaks than predicted by group theory for normal cubic spinel [25-27]. The new features in Raman and IR-spectra of inverse or partially inverse spinels can be considered as a result of growing disorder that can lead to splitting of the degenerated Raman modes of $Fd\bar{3}m$ space group, as well as activation of the silent and zone-boundary modes. But the main reason for the appearing of new

modes in single crystals (or bulk) is a change of local symmetry [28]. In a detailed study by polarized Raman spectroscopy and comparison with lattice dynamics calculations Ivanov at al. [29] show that the local ordering in $NiFe_2O_4$ is most probably of tetragonal *P4122/P4322* symmetry and that the orthorhombic *Imma* structure "cannot be definitively ruled out" due to the good correspondence of some calculated frequencies to experimentally observed bands. Spectra obtained by superposition of scattering from different combinations of tetragonal and orthorhombic symmetry structures give in average a cubic symmetry.

In a later paper, Iliev at al. [30] also point out that from the symmetry consideration, some of Raman's modes of *P4122* site symmetry directly correspond to Γ-point modes of $Fd\bar{3}m$, whereas the rest of the modes originate from a zone folding, which maps the zone-boundary *X*-point of $Fd\bar{3}m$ onto the Γ-point of *P4122*. Therefore, we will consider it justified to describe the vibrational modes in the spectra of disordered nanoferrites as modes of $Fd\bar{3}m$ symmetry.

3.2.1. Raman modes of $CoFe_2O_4$ nanoparticles - comparison with other oxide spinels

The Raman spectra of predominantly inverse cobalt ferrite are expectedly richer than for an ideal spinel structure of $Fd\bar{3}m$ symmetry (where one expects five peaks (two modes (A_{1g} + E_g) in the XX polarization and three F_{2g} modes in the XY polarization). However, the highest-energy Raman mode is completely divided and instead of five "main" peaks, as in other inverse ferrites, in Raman spectra of cobalt ferrite exist six in Raman spectra of cobalt ferrite exist six (at least). The corresponding "main" peaks in the micro-crystalline $CoFe_2O_4$, are $F_{2g}(1)$ at 210 cm^{-1}, E_g at 312 cm^{-1}, $F_{2g}(2)$ at 470 cm^{-1}, $F_{2g}(3)$ at 575 cm^{-1}, $A_{1g}(2)$ at 624 cm^{-1} and $A_{1g}(1)$ at 695 cm^{-1} [31]. In films of $CoFe_2O_4$ thicker than 100 nm, wave numbers of main peaks are almost the same as in the bulk [32]. Dissociated $F_{2g}(1)$ peak is also seen in Raman spectra of crystalline samples. In Ref. [33] are registered peaks at: 160, 207, 304, 473, 570, 615 and 693 cm^{-1}. The first two peaks are of $F_{2g}(1)$ symmetry.

Room temperature Raman spectra of the cobalt ferrite nanoparticles are presented in Fig. 2. From the top to the bottom are the spectra of nanoparticles with increasing values of the lattice constant and decreasing value of the coefficient of the inversion. It can be seen that with a decrease in the degree of inversion there is a decrease in the intensity of the Raman spectra due to an increase in the disorder in the crystal lattice. Although spectra are of relatively low intensity, all modes except $F_{2g}(3)$ are clearly visible. The modes are almost symmetrical and can be fitted by Lorentzians. As we have already seen from XRD characterization, all investigated $CoFe_2O_4$ samples, obtained by various synthesis techniques, showed a typical XRD pattern of $Fd\bar{3}m$ space group. As nanoparticle samples of $CoFe_2O_4$ are macroscopically cubic, their Raman

modes are assigned as in normal cubic spinel, according to *Eq.* (1). Wave numbers of Raman modes are $F_{2g}(1)^* < F_{2g}(1) < E_g < F_{2g}(2) < F_{2g}(3) < A_{1g}(2) < A_{1g}(1) < A_{1g}^*$, Table 1. The modes in the spectra of nanoparticles have a predictable shift towards lower wave numbers compared to the bulk [26, 34-37].

Figure 2

Table 1

In the partially inverse cobalt ferrite the mass, the different ionic charges and the differences in ion-radius between Fe^{3+} and Co^{2+} cations split the A_{1g} mode into two branches: $A_{1g}(1)$ and $A_{1g}(2)$. Mode with the smallest wave number, $F_{2g}(1)$, that originates primarily from translation vibrations of tetrahedrons, is divided also – into modes $F_{2g}(1)^*$ and $F_{2g}(1)$. Translation vibrations of Fe^{3+}- O_4 produces $F_{2g}(1)$ mode and it can be supposed that translation vibrations of heavier Co^{2+}- O_4 tetrahedrons in partially inverse cobalt ferrite gives mode at lower wave numbers $F_{2g}(1)^*$. This $F_{2g}(1)^*$ modes do not appear in the Raman spectra of single crystals of spinels with a perfect structure and ideal degree of the inversion (x=0, or x=1). There is no consensus in the literature on the origin of Raman vibrational modes in cubic spinel oxides, but modes A_{1g} and $F_{2g}(1)$ in ferrites are considered to have the smallest contribution from octahedral vibrations.

In spinel ferrites A_{1g} modes are clearly connected with oscillations in the tetrahedrons. But, in the case of chromites and aluminates, this mode incomparably more depends on octahedral-related oscillations [16]. In Fig. 3a), the Raman spectra of the various bulk ferrites are shown. The following spectra were taken from the literature: $MgFe_2O_4$: Ref. [16], $CoFe_2O_4$: Ref. [31], $NiFe_2O_4$: Ref. [34] and almost normal $ZnFe_2O_4$: Ref. [36]. In Fig. 3a) it is visible that even the shape of A_{1g} mode in partially inverse ferrite suggests a great influence of tetrahedral vibrations. Namely, modes in which the reduction of inversion leads to the appearance of a larger "satellite" peak (a peak whose presence depends on the divalent cation M = Mg, Fe, Co, Ni, Zn) obviously have dominant contribution of tetrahedral vibrations. Nakagomi *at al.* [38] showed that a cation inversion in $Mg_xFe_{3-x}O_4$ estimated from areas of corresponding parts of A_{1g} Raman peak is in a good agreement with the results obtained by XRD and Mössbauer spectroscopy.

Figure 3

This is also applicable to other inverse spinels, but most often the proportion should be corrected by some factor characteristic for the given crystal. In the case when A_{1g} mode is predominantly connected with octahedral stretching vibrations, like in aluminate spinels, the appearance of an additional A_{1g} mode at low wave numbers means that part of the Al^{3+} cations has moved into tetrahedral positions. In a similar way, from the intensity ratio of the two A_{1g} modes, the degree of inversion can be estimated (with the corresponding correction coefficient) [39].

Comparing with other oxide spinels, such as mostly normal chromites and aluminates [16], as well as with cobaltites, shown in Fig. 3b) (two normal - three inverse), we can see that in each of these spinel groups the values of wave numbers of A_{1g} modes vary in some range characteristic for trivalent cation. In Fig. 2b) are presented Raman spectra taken from the literature: $MgCo_2O_4$ [40], $FeCo_2O_4$ [41], $CoCo_2O_4$ [42], $NiCo_2O_4$ [41] and $ZnCo_2O_4$ [43, 44].

In fact, excluding the $F_{2g}(1)$ mode in oxide spinels, all other modes follow a pattern dictated by octahedral trivalent cations for x=0, or octahedral complex for $x\neq0$. Raman spectra of normal and partially inverse and inverse spinels look very similar. Among all oxide spinels it is the most evident in the spectra of cobaltites. In ferrites and cobaltites with M^{2+} different from Fe^{2+} or Co^{2+}, respectively, Raman modes can be directly compared to the corresponding modes of the isostructural magnetite $FeFe_2O_4$ and the cobaltite $CoCo_2O_4$, respectively. It seems that one peak in dominantly inverse ferrites with a doublet-like structure represents the unit cell with all Fe ions and that the other one is due to the unit cell with M^{2+} ions. The same is in the case of cobaltites and other spinels especially when there exists a deviation from the ideally arranged spinel structure ($x\neq1$, or $x\neq0$). Spectra of CoB_2O_4 and MgB_2O_4, where B^{3+}= Al, Fe, Co, presented in Fig. 3c) and Fig. 3d), respectively, show that the influence of divalent cations on the general characteristics of Raman spectra and the wave numbers of the main modes is incomparably smaller than the influence of trivalent cations. In addition to the already mentioned spectra, in Fig. 3c) and Fig. 3d) are presented spectra of aluminate spinels: $MgAl_2O_4$ taken over from Ref.-s [39], [45], $CoAl_2O_4$ [46], and spectrum of $MgFe_2O_4$ (with smaller inversion) from Ref. [37].

It is obvious from the Fig. 3d) why $F_{2g}(1)$ mode is assigned as the translational vibration of AO_4. Its wavenumber (*ie* vibrational energy) unambiguously depends on the mass of the tetrahedron's cation(s). In Raman spectra of CoB_2O_4, Fig. 3c), due to the almost similar masses of tetrahedral cations (Co, 0.05Co+0.95Fe, Co), the $F_{2g}(1)$ modes have similar wave numbers. In Fig. 3b) mode $F_{2g}(1)$ in partially inverse $ZnCo_2O_4$ is divided in two parts. At 204 cm^{-1} is the part

that corresponds to lighter Co-O_4 tetrahedra (Co^{2+}/Co^{3+}); at 182 cm^{-1} are the translation vibrations of Zn-O_4 tetrahedra [44].

Based on the spectra of ferrites in Fig. 3a), it can be concluded that divalent cations in ferrites significantly affect the wave numbers of $F_{2g}(1)$, $F_{2g}(2)$ and $F_{2g}(3)$ modes, more than E_g mode. The component of A_{1g} mode associated with trivalent cations is also dependent on the radius of M^{2+} cation.

The weak mode $F_{2g}(3)$ is not clearly defined in our spectra of nanoparticle $CoFe_2O_4$ samples. In the deconvolution of spectra, it is simulated by one broad Lorentzian, Fig. 2. We can only assume that $F_{2g}(3)$ mode behaves like in other inverse and partially inverse ferrites. In the study on $CoFe_2O_4$ samples with wide range of particle's sizes given in the paper of Chandramohan *at al.* [31] a structure of $F_{2g}(3)$ mode is not clearly seen, also. In the spectra of $CoFe_2O_4$ nanoparticles obtained in Ref. [47] the appearance of the peak only hints at a possible doublet structure, while in the spectra of $NiFe_2O_4$ [26, 34], $MnFe_2O_4$ [25] and $MgFe_2O_4$ [16, 37] this doublet structure is clearly visible. Some of these spectra are presented in Fig. 2a). It can be seen in Raman spectra of bulk $NiFe_2O_4$ [36], as well as in the nanoparticle's spectrum, with $x \approx 1$ [26], that components of mode $F_{2g}(3)$ are clearly separated and have similar intensities. It can be supposed that mode $F_{2g}(3)$ originates from various vibration contributions. In nanoparticle $NiFe_2O_4$ samples it has been confirmed that a part of the mode at higher wave numbers increases in intensity with the rise of sintering temperature (reaching the height of the part of peak at lower wave numbers) due to a simultaneous increase in inversion [48]. Part of the $F_{2g}(3)$ peak in $MgFe_2O_4$ at higher wave numbers [37] also increases with increasing of the inversion, but stays weaker than part of mode at lower wave number. (Speaking about $MgFe_2O_4$, we must mention the intriguing difference in appearance of A_{1g} Raman modes of balk and nano-samples comparing to natural magnesioferrite crystals (see RUFF base). Only in natural crystals ($x \approx 0.95$) the part of A_{1g} mode that corresponds to tetrahedral oscillations of Fe^{3+} is at lower wave numbers than Mg-part, in accordance with higher force constant and higher mass of Fe^{3+}. In the case of synthetic $MgFe_2O_4$ crystals (and nano-crystals), with significantly lower lattice constant, many authors ascribe higher and stronger A_{1g} part to Fe^{3+}-O_4 oscillations.

We could not find in literature Raman spectra of zinc ferrite single crystal, or microcrystalline crystal with x=0. The asymmetrical feature that can be the $F_{2g}(3)$ mode, merged with $F_{2g}(2)$ mode, is seen in slightly inverse $ZnFe_2O_4$ ($0.07 \leq x \leq 0.2$) microcrystals (300 nm) obtained by Ulpe *at al.* [49, 50]. In the literature, one can find Raman spectra of zinc ferrite nanocrystals with x=0 and paramagnetic behaviour. Their Raman modes with various relative intensities and wave numbers, according to Ulpe *at al.* [49], can be connected with structure imperfections and local deviations from the spinel structure of x=0 coordination. In

comprehensive review of Galinetto *at al*. [36], the "controversial landscape" of Raman modes obtained from 12 papers is summarized. Modes of the same assignation are in very wide intervals of more than 100 cm^{-1}. Wave numbers of main modes, especially E_g and $F_{2g}(2)$ in Ref-s. [36] and [49], much better (comparing to other Ref-s.) corresponds to the trend of dependence of ferrite modes on the size of divalent cations, so we have shown the spectrum from Ref. [36] in Fig. 3a). (The structure of $F_{2g}(3)$ mode is not clearly visible even in this selected spectrum.)

The peak $F_{2g}(2)$ in the bulk ferrites (with the exception of $ZnFe_2O_4$, where this mode is not clearly separated from the neighboring $F_{2g}(3)$ band) seem to be less asymmetric, but its wave number, significantly depends on M^{2+} cation.

As we have already seen, wave numbers of all modes depend on various vibration contributions. In Fig. 4 is shown the dependence of the Raman modes in ferrites and cobaltites on the tetrahedral radius of divalent M^{2+} cations. The dependence of effective cation radius for tetrahedral ($M_{1-x}Fe_x$) and octahedral ($Fe_{2-x}M_x$) complexes is given only for ferrites. We can't find the values of cation distributions for cobaltites. All results must be considered only qualitatively due to the impossibility of finding Raman spectra on single crystals for some ferrites and cobaltites. Therefore, in the presented spectra, Fig. 3a) and b), can be found deviations in peak positions due to particle size and structural imperfections.

Figure 4

In Fig. 4a) it can be seen that the all modes in ferrites depend in some extent of M^{2+} cations: modes $F_{2g}(1)$ and $F_{2g}(2)$ the most, $F_{2g}(3)$ and $A_{1g}(1)$ somewhat less, and the mode E_g does not show a clear dependence on M^{2+} cation radius. The same trend of change of wave numbers is obtained as a function of the lattice constant of the ferrite. In Fig. 4b) the dependence of the modes on the effective radii of the tetrahedral complexes is shown. All modes of inverse and partially inverse ferrites are grouped with the modes of magnetite Fe_3O_4 (due to the predominant influence of the small tetrahedral radius of trivalent Fe^{3+}), while the modes of normal $ZnFe_2O_4$ are at the other end of the scale. In relation to the effective (mean) radius of the octahedral complexes, the dependence is more complicated, and only for the E_g mode is a clear trend of decrease of wavenumbers with an increase in the radius of the octahedral cation, as can be seen in the inset in Fig. 4b). It can be concluded that E_g modes are predominantly connected to octahedral vibrations. In the Raman spectra of cobaltites (Fig. 3b) and in Fig. 4c)) is visible that all modes show very little dependence on the radius of M^{2+} cations. There is a specific situation in cobaltites due to possible presence of Co^{2+} cations both in octahedra and tetrahedra [51]. In dominantly normal spinels $CoCo_2O_4$ and $ZnCo_2O_4$ it seems that Co^{3+} cations are mostly

in octahedra. It suggests magnetic measurements. In the octahedral sites are low spin Co^{3+} (S=0) and magnetization of Co_3O_4 originate only from Co^{2+} [52]. Magnetization of normal cobaltites (with ideal structure) should depend only on spin of M^{2+} cation. Bulk samples of $ZnCo_2O_4$ show weak paramagnetism due to vacancies or structural defects, but nanoparticles can be even weak ferromagnetic - depending on the way of synthesis, size effect, surface spin disorder, and shape anisotropy [53]. Origin of the mentioned ferromagnetism in $ZnCo_2O_4$ can be a partial inversion, *i.e.* presence of high spin Co^{3+} cations in tetrahedral sites.

E_g modes are in characteristic narrow interval of wave numbers in all oxide spinels: for mostly normal aluminates about 404±8 (4%) cm^{-1} and for chromates about 445±5 cm^{-1} (4%) and show a slight decrease with increasing of M^{2+} ion radius [16]. In ferrites is E_g = 323±17 cm^{-1} (10%) and in cobaltites about 480±5 cm^{-1} (2%), see Figs. 4a) and c). The increased dissipation of the wave numbers in ferrites and cobaltites, due to the use of the spectra of non-mono-crystal samples, screen the dependence on the size of M^{2+} cations expected in inverse spinels. But, according to graph in the insert of Fig. 4b), it is obvious that the values of E_g modes mainly depend on the effective radius of the octahedral complex, R_{oct} = 1/2R($Fe_{2-x}M_x$). Based on Fig. 3, it seems that the impact of divalent cations on E_g modes of ferrites and cobaltites is similar as in other oxide spinels.

From a comprehensive review by D'Ipolito *at al.* [16] and from the Raman spectra of various references given in this paper, it is visible that F_{2g}(2) modes of ferrites and chromates, although predominantly dependent on octahedral vibrations, "feel" the greater influence of tetrahedral cations than in aluminates and cobaltites.

As we have seen, the vibrations of the oxygen anions bound to Fe^{3+} and M^{2+} cations in the inverse ferrites can be superimposed in one band, like in E_g and F_{2g}(2) modes, or can be separated, like in A_{1g} and F_{2g}(1) modes when the vibrational wave numbers of characteristic units are sufficiently different. Modes F_{2g}(3) in ferrites have more complex "structure". A peak shoulders visible in the Raman spectra of the inverse cubic spinels are due to altered local symmetry, but can depend on share of various cation contributions to certain mode, also. In the case of $NiFe_2O_4$ single crystal, with x=1 a clearly visible shoulder A_{1g}(2) is connected only with change in local symmetry [34]. This may be a confirmation that the oscillations in A_{1g} mode are not only tetrahedral, but represent a combination of tetrahedral and octahedral contributions. The shoulder can be interpreted as the contribution of octahedral oscillations.

In mainly normal II-III ferrites like $ZnFe_2O_4$, $MnFe_2O_4$ [54, 55], or $CdFe_2O_4$ [56], it is visible that A_{1g}(2) part of mode at lower wave numbers is dominant and very broad. As we have already seen, theoretical calculations for $ZnCr_2O_4$ [23], showed that Cr-O_6 and Zn-O_4 similarly participate in potential energy, and experimental Raman spectra of normal chromates [16], show

almost the same values of A_{1g} wave numbers (~2%) regardless to M^{2+} cation. It means that stretching vibrations of octahedra Cr-O_6 could be dominant in the A_{1g} mode of chromates. Bearing this in mind, it can be assumed that the $A_{1g}(2)$ mode of mostly normal ferrites also largely originates from octahedral Fe-O_6 stretching vibrations. Kreisel *at al.* [57], based on extensive experimental experience, also see the origin of the A_{1g} mode of normal ferrites in Fe-O_6 oscillations. Wave number of $A_{1g}(2)$ mode in $ZnFe_2O_4$ is 646 cm^{-1} [36], for $MnFe_2O_4$ is 622 cm^{-1} [54] and in $CdFe_2O_4$ is 635 cm^{-1} [56]. Neither the mass nor the tetrahedral ionic radius of the M^{2+} cation clearly affects the wave number of $A_{1g}(2)$ mode. Dominant $A_{1g}(2)$ peaks in various normal ferrites differ by less than 4%. It is possible that almost double FWHM of $A_{1g}(2)$ mode compared to $A_{1g}(1)$ in both normal and inverse ferrites originates from the superposition of Fe-O_6 and M^{2+}-O_4 contributions.

Briefly, the attractive idea that part of the oscillations in some mode may be related to oxygen oscillations in Fe-O or *M*-O bonds is not always applicable to modes in Raman spectra. It is clear why there are so many different explanations (which are not supported by lattice dynamic calculations) in the literature about the origin of various peaks.

The attribution of dominant type of oscillations to certain mode is controversial, also. The A_{1g} mode in dominantly inverse spinel ferrites is connected with symmetry stretching vibrations of oxygen anions in mainly tetrahedral bonds of Fe^{3+}-O_4, or ($M_{1-x}Fe_x$)-O_4. If x<1, in A_{1g} mode occurs a decoupling of M-O_4 and Fe-O_4 tetrahedral oscillations. For all the other Raman modes, there are some disagreements about their assignments. For example, according to Ref-s. [37, 49, 58], mode $F_{2g}(3)$ is attributed to asymmetric bending of the Fe(*M*)-O bonds. Mode $F_{2g}(2)$ is due to the asymmetric stretching of the Fe(*M*)-O octahedral bonds and the mode E_g is attributed to symmetric bending of the Fe(*M*)-O tetrahedral bonds [37, 58]. Shebanova and Lazor [59] believe that $F_{2g}(2)$ is associated with asymmetric stretching of oxygen bonds to Fe^{3+} cations, *i.e.* with tetrahedra. According to Bera *at al.* [60] $F_{2g}(3)$ is an asymmetric stretching of tetrahedron, $F_{2g}(2)$ asymmetric stretching in octahedron and E_g is symmetric bending. All authors agree that $F_{2g}(1)$ mode is related with translations of tetrahedrons. However, most authors believe that Raman modes below 600 cm^{-1} in spinel ferrites (except $F_{2g}(1)$) are generally associated with octahedral [31, 61].

In this paper, it is shown in comparison with other ferrites and other oxide spinels, that the E_g mode is primarily associated with oscillations in the octahedral environment. In both normal and partially or fully inverse ferrites, the wavenumbers of the E_g modes have similar values. This means that the E_g modes have similar force constants and similar effective cation radius, which is only possible for an octahedral complex. In the octahedral complex, the much smaller Fe^{3+} radius considerably affects the average radius, so it is similar to normal Zn-ferrite (with Fe^{3+} in

octahedra), see Fig. 3a). If this mode were predominantly dependent on tetrahedral oscillations, its value in normal Zn-ferrite (with large Zn^{2+} in tetrahedra) would be significantly lower than in inverse ferrites with small Fe^{3+} cation in tetrahedra. Wave numbers of E_g modes in normal ferrites are: in Zn-ferrite 340 cm^{-1} [36], in Mn-ferrite 324 cm^{-1} [54], or 331 cm^{-1} [55] and in Cd-ferrite 329 cm^{-1} [56], similar to the E_g wave numbers of inverse ferrites (306-333 cm^{-1}, Fig. 4 a).

It has also been shown that in ferrites $F_{2g}(3)$ mode has complex "structure" that is dependent on radius of M^{2+} cations. At the same time, in Figs. 3c) and Fig. 3d) is visible a conspicuous dependence of $F_{2g}(3)$ mode on the trivalent (octahedral) cation. Mode values of the omitted partially inverse $MnFe_2O_4$ ferrite [25] confirm this claim.

As we have seen, the appearance of the Raman spectra of ferrites (like all cubic spinels) is decisively influenced by the trivalent cation, i.e. octahedral complex (whose average radius is close to that of a small trivalent cation). This is evident from the Raman spectra presented in this paper, as well as in Ref. [16]. The exception is the $F_{2g}(1)$ mode, which largely depends on the oscillation of the entire tetrahedra, so its wave number is also affected by the mass of the tetrahedral cations. In the spectra of inverse ferrites, there is a noticeable separation in two modes: A_{1g} and $F_{2g}(1)$. Dissociation of modes is possible only in those modes in which there is more influence of tetrahedral oscillations. In that case, "independent" oscillations can occur in tetrahedra with M^{2+} and Fe^{3+} cations. With octahedral modes, such a separation is unlikely, because the octahedra form a tightly connected network. The tetrahedra are separated from each other, so it is possible to uncouple the oscillations of anions bound to different cations.

Raman spectra of all cobaltites look very similar and confirm already mentioned mode behaviour as in other oxide spinels. In partially inverse cobaltites, only the A_{1g} and $F_{2g}(1)$ modes are asymmetric, or even separated. (See spectrum of $ZnCo_2O_4$, from Ref. [44], Fig.3b).

It is possible that the $F_{2g}(3)$ mode of ferrite has a significant part of tetrahedral oscillations, because this mode looks like a partially dissociated (doublet) mode in some spectra.

In Table 1 are wave numbers of deconvoluted modes from Raman spectra of the investigated $CoFe_2O_4$ nanoparticles obtained by various synthesis procedures. The values of wave numbers are generally in accordance with literature [47, 62]. It can be seen that the higher values of wave numbers correspond to the samples with bigger nanoparticles. In our investigation, with nano-particles of similar sizes, this is visible only for $A_{1g}(1)$ mode and $F_{2g}(1)$ mode. Nano material obtained by micro-emulsion method, "ME", with the biggest nanoparticles, has the highest wave number of $A_{1g}(1)$ mode and "US-CO" obtained by ultrasonically assisted coprecipitation - the smallest.

Generally, asymmetry and dissociation of Raman modes is characteristic for inverse and partially inverse spinel structure of lower symmetry, but such striking separation of A_{1g} mode is

observed only in cobalt ferrite. The separation of the A_{1g} mode in two distinct parts (by about 70 cm^{-1}) is an outstanding feature of Raman spectra of cobalt ferrite. The mode marked with $A_{1g}(1)$ refers to the symmetric stretching of Fe^{3+} - O bonds in tetrahedrons and $A_{1g}(2)$ to the stretching of Co^{2+} - O bonds in tetrahedrons. Weak A_{1g}* mode matches to the vibration of Fe^{3+} in incomplete tetrahedrons, as in maghemite. This specificity of the spectra implies that the ordering of cations is much better in tetrahedral positions than in octahedral ones. Consequently, due to the separation of Fe-O and Co-O oscillations, it is possible to estimate the degree of cation inversion (x_R), i.e. the Fe-content in the tetrahedral (A) site, as follows:

$$x_R = I_{A1g(1)} / [(I_{A1g(1)} + S \cdot I_{A1g(2)})]$$

where $I_{A1g(1,2)}$ are corresponding Lorentzian integrated areas and S - represents the relative oscillator strength of the Co^{2+}–O bonds with respect to the Fe^{3+}–O bonds in tetrahedrons.

The force constant k, which governs the mode frequency $\omega^2 \propto k/m$, where m is the reduced mass of ions, is directly proportional to the charges Z_A and Z_O of the central ion A and oxygen, respectively and inversely proportional to the cube of the associated bond length R_{tet} (= $r_A + r_O$), as $k \propto Z_A Z_O / R_{tet}^3$ [30]. The ionic radii of tetrahedral Co^{2+} and Fe^{3+} ions are 0.58 Å (high spin) and 0.49 Å (high spin), respectively and radius of oxygen O^{2-} in tetrahedrons is 1.38 Å [63]. Therefore, relative oscillator strength of the Co^{2+} bonds with respect to the Fe^{3+} bonds in tetrahedrons is:

$$S = [Z_{Co}/R_{Co\text{-}O}^3]/[Z_{Fe}/R_{Fe\text{-}O}^3] = 0.58$$

Calculated Fe contents, x_R, in tetrahedral site for various cobalt ferrite samples are given in Fig. 2 and shown graphically as the function of corresponding lattice constant in Fig. 5. It can be seen that Fe content in A-site estimated from Raman spectra is in good accordance with the degree of inversion obtained by XRD analysis.

Figure 5

3.2.2. FIR Reflectivity

The IR reflectivity spectra of $CoFe_2O_4$ nanoparticles obtained by various synthesis techniques are shown in Fig. 6. It is visible that spectra have more than four F_{1u} modes predicted by factor group analysis for normal cubic spinels, *Eq*. (1). The main modes are assigned as in normal spinel. Satellite peaks are noticeably weaker. They are indicated by arrows. The spectra are of relatively good intensity. The intensity roughly corresponds to the nanoparticle sizes of the tested samples.

Figure 6

In general, the number of vibration mode increases by cancelling of degeneracy due to crystal lattice disordering, or the existence of defects and oxygen vacancies. Cation inversion does not cause a macroscopic change in symmetry - these inverted cations stay equivalent for the group theory, but it do not imply a vibrational equivalence. If the masses, charge, or the cation-oxygen bonding forces, are sufficiently different, the distinct absorption bands in the spectrum will appear. According to *Eq*. (2), in addition to anions, A- and B-cations also participate in oscillations. Values of the wave numbers of the main modes reflect the change in the mean values of the effective charges in the A and B sites, as well as the change in the mean lengths of the tetrahedral and octahedral bonds.

As we have seen in the conclusions of the theoretical calculations [23], all mods are combinations of different contributions. In normal spinels the highest-frequency band cannot be assigned to either the tetrahedral or the octahedral groups. This mode predominantly arises from the oscillations of the anions bonded to cation with the highest valence [17]. For normal $ZnCr_2O_4$ octahedral B-X stretching with trivalent cation contributes to this mode to a greater extent comparing to A-X stretching vibrations [23]. The force constants essentially depend on the valence of the cation, so in the vibrations of the high-energy mode a greater contribution makes oscillations of trivalent cation in octahedrons. Preudhomme and Tarte investigated the absorption spectra of numerous normal spinels [18] and show that two highest modes predominantly depend on oscillations of anions bonding to octahedral cations. Dependence on tetrahedral M^{2+} cations is visible, but it couldn't be possible to define its nature. The influence of the cation mass is clearer in the modes in which the cations themselves participate more in the oscillations. In Ref. [21] was shown that oscillations of both cations are weak in the highest, $F_{1u}(4)$ mode. In $F_{1u}(3)$ mode octahedral cations contribute more. In the remaining weak modes, masses of cations have very clear influence: mass of octahedral cation in $F_{1u}(2)$ mode and the mass of M^{2+} has a dominant influence in $F_{1u}(1)$ mode.

In a hypothetical situation - if $ZnCr_2O_4$ were inverse, with trivalent Cr^{3+} in tetrahedrons, k_t force constant would be 6/4=1.5 times greater and k_o 5/6=0.83 times weaker, which would significantly increase the share of A-X stretching in the energy of mode with the highest wave number. In the case of the inverse ferrites, with Fe^{3+} in tetrahedrons, $F_{1u}(4)$ mode may be assigned to the antisymmetric stretching of the FeO_4 tetrahedron, prevalently. There are many experimental results that undoubtedly confirm that in the $F_{1u}(4)$ mode of inverse ferrites oxygen oscillations in Fe^{3+} tetrahedra dominate, and that in the $F_{1u}(3)$ mode the X-oscillations oscillations in the octahedral complex have the greatest influence.

In Ref. [64] are given IR spectra of $CoCr_xFe_{2-x}O_4$, with $0 \leq x \leq 1$. The Rietveld analysis showed that there were no major changes in the amount of Fe^{3+} cations in the A-site, only about 10%, while Cr is mounted only in the B-site. The small change in A-site was accompanied by a small change in the value of the wave number of the highest-frequency band, while in the structure and wave number of the next lower mode, there were noticeable changes. This result confirms that the high-frequency band is predominantly dependent on oscillations of oxygen in Fe^{3+}- tetrahedra. The next IR band is connected mostly with oscillations in Fe^{3+} and Cr^{3+} octahedrons. Patange *at al.* [65] for $NiCr_xFe_{2-x}O_4$, with $0 \leq x \leq 1$, also showed that the greatest changes were seen in octahedral complex, i.e. mode $F_{1u}(3)$. Substitution with Cr, which has an affinity for the octahedral position, dominantly impacts the $F_{1u}(3)$ band.

We will now look at the influence of Zn, which has an affinity for the tetrahedral position, on the IR modes of ferrites. In Ref. [66] was investigated the influence of Zn in nanoparticles of partially inverse $Mg_{1-x}Zn_xFe_2O_4$ ($0.3 \leq x \leq 0.7$). In FTIR spectra were clearly seen two fundamental spinel bands. IR band at higher wave numbers has shift toward lower wave numbers with the increasing of Zn content (565 cm^{-1} → 545 cm^{-1}) and lower band shifts towards higher wave numbers (435 cm^{-1} → 441 cm^{-1}). This change resulted from the incorporation of Zn^{2+} ions in tetrahedral site instead smaller Fe^{3+} cations (and Mg^{2+} cations in smaller extent). Tetrahedral bonds, R_{tet}, increase, force constants become weaker and a mode connected with tetrahedral oscillations exhibits a red shift. The movement of Fe^{3+} ions from A-site to B-site leads to increase of force constants of octahedral oscillations due to increase of effective charge and this resulted in blue shift of corresponding IR mode. Tatarchuk at al. [67] investigated $Co_{1-x}Zn_xFe_2O_4$ ($0 \leq x \leq 1$) nanoparticles. Based on XRD and Mössbauer spectroscopy, it can be seen that with increasing amount of incorporated Zn, the amount of Co^{2+} primarily decreases in octahedra (slightly in tetrahedra). Zn actually "pushes" significantly smaller Fe^{3+} cations from tetrahedra to octahedra. In the FTIR transmission spectra, the replacement of cobalt with larger zinc is accompanied by a decrease in the wave numbers in the ferrite mode with the highest wave number, *i.e.* the mode that arose in the oscillation of the tetrahedral complex. The next strong mode, which shifts to higher wave numbers with increasing Zn, is unambiguously related to octahedra, as is previously explained for the case of $Mg_{1-x}Zn_xFe_2O_4$.

To analyse the reflectivity spectra of nanoparticle $CoFe_2O_4$ samples obtained by different synthesis methods and estimate the positions of characteristic transverse and longitudinal frequencies we used a Decoupled Plasmon - Phonon (DPP) model of the complex dielectric function $\varepsilon(\omega)$ to simulate reflectivity spectra $R(\omega)$ [68, 69]:

$$R(\omega) = \left| \frac{\sqrt{\varepsilon(\omega)} - 1}{\sqrt{\varepsilon(\omega)} + 1} \right|^2 \quad (3)$$

$$\varepsilon(\omega) = \varepsilon_{\infty}\left[\prod_j \frac{\omega_{LOj}^2 - \omega^2 + i\cdot\omega\cdot\gamma_{LOj}}{\omega_{TOj}^2 - \omega^2 + i\cdot\omega\cdot\gamma_{TOj}} - \frac{\omega_p^2}{\omega^2 - i\cdot\omega\cdot\gamma_p}\right] \quad (4)$$

In the formula above, ε_∞ is the high-frequency dielectric constant, ω_{LOj} and ω_{TOj} are longitudinal and transverse wave numbers of the *j*-th oscillator, γ_{LOj} and γ_{TOj} are their corresponding dampings, ω_p is the plasma wave number and γ_p is plasma damping. The first term in *Eq.* (4) is the lattice vibration contribution for coupled phonon modes with the asymmetry of the dampings of TO and LO wave numbers, whereas the second term is the Drude term for the free-carrier contribution to the dielectric constant. Bulk $CoFe_2O_4$ is a good insulator, but Drude contribution must be added to fit properly the nanoparticle spectra.

$CoFe_2O_4$ nanoparticles have a semiconducting behaviour. The total conductivity at temperatures below 400 °C is dominated by the grain boundary contribution. Conductivity arises from hole hopping between Co sites. At higher temperatures the conductivity rises additionally due to electron hopping between the Fe sites of the lattice [70].

All spectra are fitted by DPP model with four main modes (+1) and a Drude term. In Fig. 6, all additional weak peaks are indicated by arrows, but they are not fitted, except the mode marked as $F_{1u}(1)$*, which is clearly visible in all spectra. Fitting parameters are given for all spectra and on a separate graph is presented the dependence of TO (and LO) oscillations on the degree of the cation inversion.

In the reflectivity spectra of nanoparticle samples of $CoFe_2O_4$ the highest-frequency band, $F_{1u}(4)$, centred from 567 to 574 cm^{-1} correspond dominantly on vibrations of oxygen anions in tetrahedral Fe^{3+}-O bonds. The value of ω_{TO} wave number increases slightly with the increase in the degree of inversion, *i*.e. with the increase in the effective charge of the tetrahedral complex. The little shoulder at slightly lower wave numbers, and even smaller shoulder at slightly higher wave numbers, probably corresponds to oscillations in deformed, and incomplete tetrahedrons, respectively.

The next strong band, $F_{1u}(3)$, can be assigned to vibration of oxygen in the octahedron's complex. Bands with ω_{TO} from 356 → 355 cm^{-1} correspond to oscillation of oxygen in Fe^{3+}- O octahedral bonds. The value of ω_{TO} slightly decreases with increase of the degree of inversion, *x*. As *x* increases, the amount of Fe^{3+} cations (and the average charge) in the octahedral sites decreases, which leads to a decrease in the force constant and wave number of octahedral oscillations.

Mode $F_{1u}(2)$ at about 305 cm^{-1} is partially masked by the close frequency of the broad $F_{1u}(3)$ mode. $F_{1u}(2)$ mode is better visible in reflectivity spectra of $NiFe_2O_4$ [26, 71, 72]. By fitting procedure we obtained very weak mode with ω_{TO} which decreases with increasing inversion from 309 → 304 cm^{-1}. This trend is expected for oscillations in the octahedral

complex. In many works, the $F_{1u}(2)$ mode is attributed to the oscillations of oxygen bound to divalent cations in the octahedra. Because the ratio of force constants of oscillations of trivalent and divalent cations: $[Z_{Fe}/(R_{Fe\text{-}O})^3] / [Z_{Co}/(R_{Co\text{-}O})^3] = 1.73$ is proportional to the squares of the corresponding wave numbers, a simple calculation shows that compliance is rather good ($355^2/304^2 = 1.36$). (According to the same calculation, the oscillations of oxygen bound to divalent Co in the octahedra could be expected to be around 270 cm^{-1}). In normal $ZnFe_2O_4$ mode $F_{1u}(2)$ is relatively strong, see Ref. [72], and it certainly cannot be attributed to the oscillation of oxygen and divalent cations in the octahedra. Some authors attribute this mode to bending vibrations [73], but it is generally accepted that the low-frequency modes $F_{1u}(2)$ and $F_{1u}(1)$ originate from complex vibrations involving both tetrahedral and octahedral groups and significant displacement of cations. According to Ref. [23], for instance, in the case of $ZnCr_2O_4$, in $F_{1u}(2)$ translation mode the contributions of A-X stretching, B-X stretching and B-B repulsion are almost equal, while in $F_{1u}(1)$ mode the translation with A-X stretching predominates.

In the investigated $CoFe_2O_4$ nanoparticle samples the lowest mode is divided in two parts: one very weak, $F_{1u}(1)$*, at 134.5-144.8 cm^{-1}, and the other, little stronger, $F_{1u}(1)$, at 176.5-181.5 cm^{-1}. Wave numbers of both modes also decrease with the increase of inversion. The part of mode at lower wave numbers is probably connected to vibrations of cation with higher mass. $F_{1u}(1)$ doublet is seen in $NiFe_2O_4$ reflectivity spectra, also [26, 71, 72]. Based on the intensity ratio of these two modes, it can be assumed that they are related to tetrahedral vibrations because the intensity of the mode associated with the heavier Co^{2+} cation (as in the case of $NiFe_2O_4$) weakens with increasing inversion.

Changes in the wave numbers of LO oscillations follow changes in TO oscillations with a change in the degree of inversion.

We have seen that by fitting the reflection spectra information is obtained about the influence of the degree of inversion of cations on the details of the appearance of the spectra as well as on the values of the main modes, i.e. the trend of shifting their values with the change of the degree of inversion. Recorded spectra can be fitted more precisely with all indicated weak sub - bands. But, the introduction of 43 free parameters per spectrum hides the danger of obtaining unrealistic results. Therefore, this first stage of fitting with a constraint on the principal modes was necessary, in order to establish logical boundaries. The reflection spectra fitted with 10 modes (only the spectra with the highest and lowest degree of inversion) are shown in Fig. 7. By including additional, weak modes, there was a certain (insignificant) adjustment of the values of the originally determined parameters - without affecting the trend of change as a function of the inversion coefficient. We can state that the mode values of the additional sub-bands change in accordance with the tetrahedral / octahedral complex to which they (dominantly) belong.

Figure 7

The values of TO and LO modes calculated by the fitting procedure can be compared with the values obtained by *Kramers-Krönig* (KK) analysis [74-76]. KK analysis of reflectivity spectra gives $\varepsilon_2(\omega) = Im(\varepsilon(\omega))$ and loss function, $\sigma(\omega) = - Im(1/\varepsilon(\omega))$ whose local maximums correspond to the values of ω_{TO} and ω_{LO}, respectively. The application of KK analysis requires previous spectrum smoothing and "upgrading" of the initial and final part of the experimental spectrum in order to obtain as realistic values as possible - especially for the modes at the ends of the spectrum. The result of the KK analysis is shown in Fig. 7 only for the samples US-CO and MC-CO, with the highest and the smallest degree of the inversion, respectively. The agreement of ω_{TO} and ω_{LO} obtained by fitting and by KK analysis is not ideal, but the trend of changing wavenumbers as a function of the degree of inversion remains unchanged. This graphic representation is attached for easier comparison of reflectivity measurement results with ATR-FTIR spectra of nanoparticles, which will be discussed in the next section.

Figure 8

Based on Waldron's model [20] can be calculated force constants for TO-wave numbers of dominantly tetrahedral $F_{1u}(4)$ IR modes (hereinafter ω_t) and dominantly octahedral $F_{1u}(3)$ IR modes (hereafter ω_o). We must note that in a certain number of works that cite Waldron's work, simplified formulas are used that are not in accordance with the original [77-79]. Therefore, we will again rewrite the original formulas and based on them calculate the force constants of the IC modes in the investigated $CoFe_2O_4$ nanomaterials.

Waldron's formulae for stretching force constants k_o and k_t were calculated from system equations for normal modes of vibrations [20]. Stretching force constant for octahedral surrounding, k_o, Waldron calculated from corresponding frequency ν_o ($F_{1u}(3)$) as:

$$k_o = ½ \cdot 32 \cdot M_B/(32+M_B) \cdot \nu_o^2$$

To obtain k_o and k_t in the SI system, atomic mass should be multiplied by $1.67 \cdot 10^{-27}$ [kg]. Number 32 is atomic mass of oxygen ($32=2M_O$). Linear frequency is: ν_o[Hz] $= 2\pi c \cdot \omega_o$, where the light velocity is $c = 2.998 \cdot 10^8$[m s^{-1}] and ω is a wave number in units [m^{-1}]. Effective masses of tetrahedral and octahedral cations are: $M_A = (1-x) \cdot M_{Co} + x \cdot M_{Fe}$ and $M_B = ½ \cdot [(2-x) \cdot M_{Fe} + x \cdot M_{Co}]$, respectively.

Tetrahedral stretching force constant k_t is:

$k_t = ¾\ M_A \cdot \nu_t^2 \cdot \nu/(\nu+3)$, $\nu_t = 2\pi c \cdot \omega_t$

$$\nu = \frac{64-2M_B \cdot u}{M_A},\ 4M_O = 64$$

$$u = \frac{2k_o}{M_B \cdot v_t^2 - 2k_o} = 1 \Big/ \left(\frac{32+M_B}{32} \cdot \frac{v_t^2}{v_o^2} - 1\right)$$

u and *v* are dimensionless quantities.

Tetrahedral and octahedral stretching force constants of IR modes in nanoparticle cobalt-ferrites calculated by Waldron's formulae are given in Table 2.

Table 2

Waldron obtained values k_o = 85 N m^{-1} and k_t = 166 N m^{-1} for his $CoFe_2O_4$ sample (for x=1) due to different wave numbers of ω_o and ω_t (374 cm^{-1} and 575 cm^{-1}).

Force constants can be calculated by the well-known formula:

$k = \mu \cdot (2\pi c)^2 \cdot \omega^2$,

where μ is reduced mass of bonded cation and anion: $\mu = M_{A,B} \cdot M_O/(M_{A,B}+M_O)$. Obtained force constants are given in Table 3, also. (It must not be forgotten that in both methods two strongest modes are considered to be purely tetrahedral or octahedral, respectively.)

As can be seen in the Table 3, with the decrease of inversion octahedral force constant k_o slightly increase and tetrahedral k_t decreases, as expected.

The values of plasma frequency ω_p obtained by fitting the experimental reflectivity spectra enable the estimation of the concentration of free carriers (n) in the $CoFe_2O_4$ samples: $\omega_p^2 = 4 \cdot \pi \cdot n \cdot e^2 / m^*$, where m^* is effective mass of free carriers (holes). It would be expected that a larger number of Co^{2+} cations in octahedral positions (larger x) with shorter hopping distances increases the possibility of achieving hopping conductivity. However, such a trend was not registered.

The valence bond-force constants may be used to calculate the elastic constants of the crystal, compressibility, Debye temperature and heat capacity instead of conventional ultrasonic pulse transmission technique. The molar heat capacity at constant volume, C_v, may be calculated in the Debye theory approximation by using the computed elastic constants of frequencies observed in the infrared spectrum [20, 80]. The elastic and thermo-mechanical properties are very important for the incorporation of the ferrite material into a functional device.

For the cubic crystals, in the special case of uniform compression, only two stiffness constants are independent and relevant:

$c_{11} = k_{av}/a$

$c_{12} = c_{11} \cdot \sigma/(1- \sigma)$,

where k_{av} is the average force constant, $k_{av} = (k_o + k_t)/2$; a is lattice constant. Poisson's ratio σ is the function of porosity P: $\sigma = 0.324(1- 1.043 \cdot P)$, [81, 82]. Modi *at al.* [80] consider that $\sigma \approx 1/3$ is an acceptable approximation for nanoparticle samples. In Ref. [83] is observed that nano-powder pressed pellets of $CoFe_2O_4$ have 93.5% of the theoretical density (without the use of sintering). The porosity of samples is low (6.5%) due to small size of nanoparticles and in this case, is $\sigma \approx 0.3$ and $c_{12} = 0.43 \cdot c_{11}$. The elastic moduli are depended on densities and subsequently on Poisson ratio. Our porous nanoparticle samples will have the elastic modulus smaller than in the case of non-porous materials.

Knowing stiffness constants, other elastic moduli for cubic ferrite system are estimated using the following equations [81]:

bulk modulus [GPa]: $B = 1/3\ [C_{11} + 2C_{12}]$

Young's modulus [GPa]: $E = [C_{11}\text{-}C_{12}][C_{11} + 2C_{12}]/[C_{11} + C_{12}]$

rigidity modulus [GPa]: $G = E/(2\ \sigma + 1)$.

The longitudinal acoustic wave velocity V_l [m/s] and transverse (shear) wave velocity V_S [m/s] were calculated as:

$V_l = (c_{11}/\rho)^{1/2}$

$V_S = (G/\rho)^{1/2}$

In this case of isotropic cubic materials like polycrystalline materials where the shear and longitudinal sound velocities, V_s and V_l are invariant with direction, the mean velocity V_m [m s^{-1}] is calculated by the following equation [84]:

$3/V_m^3 = 2/V_s^3 + 1/V_l^3$.

At low temperatures the vibrational excitations arise solely from acoustic modes (one longitudinal and two transversal – shear modes). One of the methods to calculate the Debye temperature θ_D is from elastic constants data, i.e. from the average sound velocity, V_m. Various methods, like the specific heat measurements, ultrasonic pulse transmission techniques, X-ray powder diffraction data analysis and infrared spectroscopy are not in general, equal and give θ_D values that can be different. (At low temperatures the Debye temperature calculated from elastic constants is the same as that determined from specific heat measurements.)

The Debye temperature θ_D can be calculated from elastic constants data, i.e. from the average sound velocity, V_m, by the following equation [84]:

$\theta_D = (h \cdot V_m/k_B) \cdot (3\rho q N_A/4\pi M)^{1/3}$,

where h is Planck constant ($h = 6.626 \cdot 10^{-34}$ J s), $\hbar = h/2\pi$, k_B is Boltzmann constant ($k_B = 1.38 \cdot 10^{-23}$ J/K), N_A is Avogadro's number ($N_A = 6.022 \cdot 10^{23}$ /mol), M is molecular weight of the $CoFe_2O_4$ (234.6 g/mol = 0.2346 kg/mol), q is number of atoms per formula unit (for present

cobalt ferrites $q = 7$), ρ is the density of the sample obtained by XRD analysis. The expression in the second bracket corresponds to $1/\lambda_{cutoff}$. Debye temperature is related to the energy of the shortest wave that can exist in crystal lattice. Shortest wave, *i.e.* high energy cut-off, has wavelength of two mean interatomic distances *d*. Since, in cubic spinel lattice with constant *a* is: $d = 1/4 \cdot (3 \cdot R_{oct} + R_{tet}) = ¼ \cdot (3a \cdot 2/8 + a\sqrt{3} \cdot 1/8) = ¼ \cdot (6+\sqrt{3}) \cdot a/8 = a \cdot 0.2416$, $\lambda_{cutoff} = 2d = a \cdot 0.4832$.

The stiffness constant c_{11}, Young's modulus *E*, rigidity modulus *G*, density ρ_{XRD}, longitudinal acoustic velocity V_l, transverse velocity V_s and mean elastic velocity V_m, together with Debye temperature obtained by combining results of IR and XRD spectroscopy, are given in Table 3. Values obtained with force constants obtained by Waldron's model are systematically lower.

Table 3

In Fig. 9a) are presented stiffness constant c_{11} and elastic constants: B, E and G obtained from directly calculated force constants. In Fig. 9b) are values of Debye temperatures obtained by elastic constant method (grey symbols) and by the IR frequency method (purple symbols), which will be discussed in the following text. For elastic constant method, previously directly calculated force constants lead to higher values of Debye temperatures. Lower force constants estimated by Waldron's model (see Table 3) give 14% lower values of Θ_D.

Figure 9

As can be seen from given formulae, stiffness constant and elastic constants depend on the average force constant of IR modes. With the increase of the inversion, TO wave number of dominantly tetrahedral mode increases faster than the wave number of octahedral mode reduces (see Table 2), what leads to the slight increase of average force constants and all elastic constants, too.

A slight increase in the XRD specific density with an increase in the inversion coefficient, which affects the decrease in the mean speed of elastic waves and the Debye temperature, leads to an additional slowdown in the growth of the Debye temperature as a function of the inversion coefficient. The value of Θ_D, calculated using elasticity constants, i.e. the speed of propagation of elastic waves and specific densities of materials obtained on the basis of IR and XRD measurements, is practically constant. Debye temperature with values $\Theta_D \approx$

616.5 → 617 K (~ 429 cm^{-1}) are obtained if force constants are calculated by formula $k = \mu \cdot (2\pi c)^2 \cdot \omega^2$. When the force constants are estimated by Waldron's model, estimated Debye temperatures are 14% lower: $\Theta_{D(W)} \approx 530.2 \rightarrow 531.8$ K (~ 369 cm^{-1}). In parenthesis are given equivalent of Θ_D in wave numbers (1K ~ 0.695 cm^{-1}). Waldron suggests that this equivalent wave number is approximately an average of the *oxygen vibration* cut-off (tetrahedral ω_t) and *cation vibration* cut-off ($\omega_{F1u(2)} = \omega_3$):

$$\omega_{av} = ½ \cdot (\omega_t + \omega_3)$$

For our samples this average values are about 439 cm^{-1}, and equivalent in temperature Θ_D is 631.3 K, slightly higher than the values obtained by elastic constant method.

Unfortunately, there are very few results of measuring the reflectivity spectrum (in FIR and MIR range) or absorption/transmission IR spectra in the FIR range, where there are visible modes connected with oscillation of cations: $F_{1u}(1)$ and $F_{1u}(2)$ (Waldron's ω_3). In Table 4 are listed values of stiffness constants c_{11} and Debye temperatures obtained in this work for $CoFe_2O_4$ samples and results for other ferrite samples estimated by elastic constants method and IR method (based on the data provided in the cited references [20, 26, 68, 81-84]).

Table 4

It can be seen from the Table 4 that the values of the stiffness constants c_{11}, as well as the Debye temperatures Θ_D for different ferrites vary by about 10%. Such close values are expected for isomorphous compounds [89].

3.2.3. ATR-FTIR spectroscopy

ATR-FTIR spectra of $CoFe_2O_4$ nanoparticle samples obtained by various synthesis methods were recorded in the mid-infrared (MIR) region from 400 to 4000 cm^{-1}. Spectra, given in the form of ATR-Absorbance, are presented in the Fig. 10.

Figure 10

It should be recalled that ATR-absorbance is not the same as absorption spectra, although peaks in the ATR-FTIR spectrum are often misinterpreted as absorption bands. Infrared total reflection mode spectra can be transformed to absorbance spectra by applying the *Kramers-Krönig* algorithm, or by the unknown commercially available software algorithm (included in the Nicolet Omnic software package). These transformed data make possible direct visual

comparison in frequency (and line shape - partially) between obtained ATR spectra and absorption bands in transmission or absorption measurements. It was found that various software packages give absorption spectra that are more or less different from the classical absorption with KBr [90].

Since the standard acquisition in ATR measurement starts from 400 cm^{-1}, in the range of "fingerprints", where the presence of eigenfrequencies of cobalt ferrite are expected to be present, one broad IR band and a small part of the other can be observed.

Deconvolution of the part of the ATR-Absorbance spectra from 400-750 cm^{-1}, gave at least 5 peaks. This procedure facilitates the detection of superimposed oscillations in the broad bands from 400 to 500 cm^{-1} and 500-750 cm^{-1}. Peaks at 409-415 cm^{-1} and 457-462 cm^{-1} correspond to stretching vibrations of octahedral bonds between oxygen and cation complex ½[$Fe_{2-x}Co_x$]. Group of peaks 520-526 cm^{-1}, 562-572 cm^{-1} and 612-625 cm^{-1} are connected with stretching vibrations of cation complex ($Co_{1-x}Fe_x$) in tetrahedral surrounding. Deconvolution of the US-CO and MC-CO samples spectra are given as an example in Fig. 11a). Fig. 11b) shows the positions of deconvoluted modes for all samples as a function of cation inversion. It can be seen that with increasing of the inversion there is a rising trend in the wave numbers of the absorption sub-bands connected to tetrahedral stretching vibrations, $F_{1u}(4)$, and lowering of octahedral stretching vibrations, $F_{1u}(3)$. Similar trend for TO modes is also observed in the analysis of the FIR reflectivity spectra. Weak mode at about 720 cm^{-1}, suggests the presence of maghemite in the samples.

Figure 11

Obtained values of ATR-absorption peaks can be compared with the values from other absorption measurements from the literature. Murugesan *at al.* [91] have obtained the higher frequencies of absorption peaks for $CoFe_2O_4$ sample obtained by ceramic method (nanoparticles of 301 nm) comparing with sample obtained by auto combustion method (with nanoparticles of 28 nm) and probably lower coefficient of inversion. Absorption bands are registered at 590/580 cm^{-1} and 412/409 cm^{-1}. In Ref. [43] in samples that were thermally treated at 200 °C and 800 °C, the modes are observed to move to higher frequencies with increasing annealing temperature (and the degree of inversion): 414→417, 477→480, 562→575 cm^{-1}. Minimal growth of octahedral bands wave numbers is a consequence of nanoparticle's growth during annealing which lead to increase of all wave numbers. Obviously, this increase compensates for the lowering of modes owing to the decrease in effective charges in octahedral sites. Tetrahedral band shows more significant increase (additionally enlarged due to the growth of nanoparticles

during annealing). These measurements are consistent with our experimental results, but in Ref. [48] the authors claim that the absorption maxima show the opposite trend. We assume that deconvolution of the observed main broad bands would show that the frequencies of individual modes increase with increasing degree of inversion. This is also indicated by the behaviour of smaller, discrete peaks of absorption (which the authors did not consider).

In the higher frequency range in MIR spectra are observed peaks that indicate the presence of water vapour and other gases from atmosphere adsorbed on the sample during preparation or storage conditions, see Fig. 10. Peaks at 1069/1025 and 1344/1335 cm^{-1} are probably multi-phonon modes connected with tetrahedral vibrations. At about 1340 cm^{-1} can be vibration of SO_2 also. In the spectrum of the sample obtained by coprecipitation, CO, there is an additional peak at 1524 cm^{-1} that shows a trace of residual alcohol. Weak modes at 2160 cm^{-1} and 2327 cm^{-1} visible in all spectra, originate from adsorbed N_2O and CO_2, respectively.

At 1632/1626 cm^{-1} is (H–O–H) bending mode and at 3390/3340 cm^{-1} is stretching vibration of hydroxyl functional group (O-H). These two peaks judge of adsorbed water in the samples.

4. Conclusions

Cobalt ferrite $(Co_{1-x}Fe_x)^t[Fe_{2-x}Co_x]^oO_4$ nanopowders obtained by various synthesis techniques were investigated by XRD diffraction analysis, Raman and IR spectroscopy. All samples showed a typical cubic spinel XRD pattern of $Fd\bar{3}m$ space group. The obtained nanoparticles are similar in sizes (15.7-19 nm), but with different internal stresses and cation inversion coefficients due to different synthesis routes. The degree of the cation inversion (x) obtained by Rietveld analysis is in a range 0.59-0.80, or 0.58-0.85 according to XRD structural analysis. In the Raman and IR spectra are observed all of first-order Raman and IR active modes. Weak sub-bands activated by structure disorder are seen also. As nanoparticle samples of $CoFe_2O_4$ are macroscopically cubic, their main Raman and IR modes are assigned as in normal cubic spinel.

Mode A_{1g} in all Raman spectra is completely dissociated, what is a characteristic of partially inverse cobalt ferrite. The part of A_{1g} mode at higher wave numbers refers to the symmetric stretching of Fe^{3+} - O bonds in tetrahedrons and the other part correspond to the stretching of Co^{2+} - O bonds. From the intensity of deconvoluted parts of A_{1g} mode it can be estimated cation inversion. Result is in rather good agreement with the cation inversion obtained by XRD analysis.

Oscillations in spinels depend on various interactions between all ions in the crystal cell and represent a combination of contributions from octahedral and tetrahedral oscillations. From

the qualitative analysis of the Raman spectra of various ferrites and cobaltites presented in this paper and Raman spectra of chromates and aluminates from Ref. [14], it is evident that the appearance of the spectra in all cubic spinels is decisively influenced by the trivalent cation in normal spinels, i.e. octahedral complex in the inverse spinels. The exception is $F_{2g}(1)$ mode, which largely depends on the oscillation of the entire tetrahedra and mass of tetrahedral cations. In the spectra of partially inverse ferrites and cobaltites, there is a noticeable separation in the modes A_{1g} and $F_{2g}(1)$. As the octahedral sites form a "lattice of condensed octahedra", mode dissociation is relieved only in those modes in which the influence of tetrahedral oscillations is greater. Mode $F_{2g}(3)$ in some ferrites looks like a doublet and its wave number markedly depends on the radius of divalent M^{2+} ion. It can be supposed that tetrahedral oscillations play a significant role in this mode. In E_g mode, the oscillations of the octahedral complex have the maximum influence, in the $F_{2g}(2)$ mode, the oscillations of the octahedral complex also dominate, but to a somewhat lesser extent.

The dominant role of octahedral or tetrahedral oscillations in individual IR modes of spinel depends on the type of ions. In inverse oxide ferrites, tetrahedral oscillations in the $F_{1u}(4)$ mode with the highest wave number prevail, because the highest force constant corresponds to oxygen oscillations attached to the Fe^{3+} cation with the highest valence (predominant in tetrahedral positions). The $F_{1u}(3)$ mode is predominantly octahedral, while the two weak modes $F_{1u}(2)$ and $F_{1u}(1)$ are complex and largely related to the oscillation of the cations themselves. The lowest mode, $F_{1u}(1)$, in the FIR reflectivity spectra is divided into two narrow peaks, the lower of which decreases with increasing inversion, which confirms that this mode originates from tetrahedral oscillations. The analysis of the reflection spectra of $CoFe_2O_4$ nanopowders with different degree of inversion confirms the assumption about the origin of the two largest modes. Namely, TO wave number of $F_{1u}(4)$ mode increase with increasing degree of inversion, *i.e.* with an increase in the effective valence of the tetrahedral complex. The wave numbers of the main band and sub-bands of the $F_{1u}(3)$ mode decrease slightly with increasing x due to the decrease in the effective valence of the octahedral complex.

The part of crystal modes seen in ATR-FTIR spectra behaves in the same way as in reflection spectra.

Elasticity constants and Debye temperature of $CoFe_2O_4$ nanopowders were calculated based on force constants of IR modes and compared with corresponding constants of other ferrites. It was found that the stiffness constants c_{11}, as well as the Debye temperatures Θ_D for different ferrites vary by about 10%. Such close values are expected for isomorphs compounds.

Acknowledgments

The authors acknowledge funding provided by the Institute of Physics Belgrade and Faculty of Technology and Metallurgy Belgrade, through the financial support of the Ministry of Education, Science, and Technological Development of the Republic of Serbia. This research was supported by the Science Fund of the Republic of Serbia, Grant No. 7504386, Nano object in own matrix – Self composite – NOOM-SeC.

This paper is dedicated to the memory of our friend and colleague, Jelena Trajić.

References

1. T. N. Pham, T. Q. Huy, A. T. Le, RSC Adv. 10 (2020) 31622.
2. N. M. Deraz, Sci. Sinter. 52(1) (2020) 53.
3. R. Vishwaroop, S. N. Mathad, Sci. Sinter. 52(3) (2020) 349.
4. S. Torkian, A. Ghasemi,, R. S. Razavi, Ceramic Intern. 43(9) (2017) 6987.
5. N. Ennassiri, A. Roth, H. Ez-Zahraouy, M. Es-Souni, Solid State Comm. 331 (2021) 114296.
6. N. S. Gajbhiye, S. Srivastava, S. Kurian, B. R. Behta, V. N. Singh, J. Phys.: Conf. Ser. 200 (2010) 072093
7. T. Shahjuee, S. M. Masoudpanah, S. M. Mirkazemi, J. Ultrafine Grained Nanostruct. Mater. 50(2) (2017) 105.
8. K. S. Rao, G. S. V. R. K. Choudary, K. H. Rao, Ch. Sujatha, Procedia Mater. Sci. 10 (2015) 19.
9. Y. Shi, J. Ding, H. Yin, J. Alloys Compd. 308(1-2) (2000) 290.
10. M. Šuljagić, P.Vulić, D. Jeremić, V. Pavlović, S. Filipović, L. Kilanski, S. Levinska, A. Slawska-Waniewska, M. R. Milenković, A. S. nikolić, Lj. Andjelković, Mater. Res. Bull. 134 (2021) 111117.
11. J. Rodriguez-Carvajal, T. Roisnel, FullProf.98 and WinPLOTR: New Windows 95/NT Applications for Diffraction Commission For Powder Diffraction, International Union for Crystallography, Newletter, 20 (1998).
12. H. D. Lutz, J. Himmrich, H. Haeuseler, Z. Naturforsch. 45a (1990) 893.
13. P. Thibaudeau, F. Gervais, J. Phys.: Condens. Matter. 14 (2002) 3543.
14. W. B. White, B. A. DeAngelis, Spectrochim. Acta 23A (1967) 985.
15. C.M. Julien, M. Massot, Mater. Sci. Engin. B97 (2003) 217.
16. V. D'Ippolito, G. B. Andreozzi, D. Bersani, P. P. Lottici, J. Raman Spectrosc. 46 (2015) 1255.
17. J. Preudhomme, P. Tarte, Spctrochim. Acta 27A (1971) 845.
18. J. Preudhomme, P. Tarte, Spectrochim. Acta 27A (1971) 1817.
19. A. K. Kushwaha, S. S. Kushwaha, Chinese Journal of Physics 45(3) (2007) 363.
20. R. D. Waldron, Phys. Rev. 99 (1955) 1727.
21. J. Preudhomme, P. Tarte, Spectrochim. Acta 28A (1972) 69.
22. J. Zwinscher, H. Lutz, J. Solid State Chem. 118(1) (1995) 43.
23. J. Himmrich, H. D. Lutz, Solid State Commun. 79(5) (1991) 447.

24. V. N. Antonov, B. N. Harmon, Phys. Rev. B 67 (2003) 024417.
25. G. Wei, L. Wei, D. Wang, Y. Chen, Y. Tian, S. Yan, L. Mei1, J. Jiao, Scientific Reports 7 (2017) 12554.
26. Z. Ž. Lazarević, Č. Jovalekić, A. Rečnik, V. N. Ivanovski, A. Milutinović, M. Romčević, M. B. Pavlović, B. Cekić, N. Ž. Romčević, Mater. Res. Bull. 48 (2013) 404.
27. A. Milutinović, Z. Ž. Lazarević, Č. Jovalekić, I. Kuryliszyn-Kudelska, M. Romčević, S. Kostić, N. Ž. Romčević, Mater. Res. Bull. 48 (2013) 4759.
28. W. B. White, B. A. DeAngelis, Spectrochim. Acta 25A (1967) 985.
29. V. G. Ivanov, M. V. Abrashev, M. N. Iliev, M. M. Gospodinov, J. Meen, M. I. Aroyo, Phys. Rev. B 82 (2010) 024104.
30. M. N. Iliev, D. Mazumdar, J. X. Ma, A. Gupta, F. Rigato, J. Fontcuberta, Phys. Rev. B 83 (2011) 014108.
31. P. Chandramohan, M. P. Srinivasan, S. Velmurugan, S. V. Narasimhan, J. Solid State Chem. 184 (2011) 89.
32. M. Foerster, M. Iliev, N. Dix, X. Martí, M. Barchuk, F. Sánchez, J. Fontcuberta, Adv. Funct. Mater. 22 (20) (2012) 4344.
33. J. L. Ortiz-Quiñonez, U. Pal, M. S. Villanueva, ACS Omega 3 (2018) 14986.
34. A. Ahlawat, V. G. Sathe, J. Raman Spectrosc. 42 (2011) 1087.
35. L. B. Salviano, T. M. S. Cardoso, G. C. Silva, M. S. S. Dantas, A. M. Ferreira, Mater. Res. 21(2) (2018) e20170764
36. P. Galinetto, B. Albini, M. Bini, M. C. Mozzati, in “Raman Spectroscopy in Zinc Ferrites Nanoparticles”, chapter 11 of “Raman Spectroscopy”, Ed. Gustavo Morari do Nascimento, (2018). http://dx.doi.org/10.5772/intechopen.72864
37. E. Fantozzi, E. Rama, C. Calvio, B. Albini, P. Galinetto, M. Bini, Materials 14 (2021) 2859.
38. F. Nakagomi, S. W. da Silva, V. K. Garg, A. C. Oliveira, P. C. Morais, A. Franco Jr., J. Solid State Chem. 182 (2009) 2423.
39. L. Liu, X. Liu, X. Bao, Q. He, W. Yan, Y. Ma, M. He, R. Tao, R. Zou, Minerals 8 (2018) 210.
40. M. Silambarasan, P. S. Ramesh, D. Geetha, V. Venkatachalam, J. Mater. Sci.: Mater. Electron 28 (2017) 6880.
41. G. Varga, Sápi, T. Varga, K. Baán, I. Szenti, G. Halasi, R. Mucsi, L. Óvári, J. Kiss, Z. Fogarassy, B. Pécz, Á. Kukovecz, Z. Kónya, J. Catalysis 386 (2020) 70.

42. J. Singh, G. P. Singh, R. K. Jain, B. Singh, K. J. Singh, R. C. Singh, J. Mater. Sci.: Mater. Electron 33 (2022) 3250.
43. M. Silambarasan, P. S. Ramesh, D. Geetha, K. Ravikumar, H. Elhosiny Ali, H. Algarni, P. Soundhirarajan, K. V. Chandekar, M. Shkir, J. Inorg. Organomet. Polym. 31 (2021) 3905.
44. J. P. Morán-Lázaro, F. López-Urías, E. Muñoz-Sandoval, O. Blanco-Alonso, M. Sanchez-Tizapa, A. Carreon-Alvarez, H. Guillén-Bonilla, M. L. Olvera-Amador, A. Guillén-Bonilla, V. M. Rodríguez-Betancourtt, Sensors 16(12) (2016) 2162.
45. L. Basyrova, S. Balabanov, A. Belyaev, V. Drobotenko, A. Volokitina, V. Vitkin, O. Dymshits, P. Loiko, J. Phys.: Conf. Ser. 1410 (2019) 012123.
46. Y. Ding, C. C. Hu, W. Q. Sheng, K. X. Song, B. Liu, J Mater Sci: Mater. Electron 32 (2021) 22813.
47. R. S. Yadav, I. Kuřitka, J. Vilcakova , J. Havlica, J. Masilko, L. Kalina, J. Tkacz, J. Švec, V. Enev, M. Hajdúchová, Adv. Nat. Sci.: Nanosci. Nanotechnol. 8 (2017) 045002.
48. R. B. Kamble, V. Varade, K. P. Ramesh, V. Prasad, AIP Advances 5 (2015) 017119.
49. A. C. Ulpe, K. C. L. Bauerfeind, L. I. Granone, A. Arimi, L. Megatif, R. Dillert, S. Warfsmann, D. H. Taffa, M. Wark, D. W. Bahnemann, T. Bredow, Z. Phys. Chem. 234(4) (2020) 719.
50. L. I. Granone, A. C. Ulpe, L. Robben, S. Klimke, M. Jahns, F. Renz, T. M. Gesing, T. Bredow, R. Dillert, D. W. Bahnemann, Phys. Chem. Chem. Phys. 20 (2018) 28267.
51. H. Chen, J. Wang, Xingrong Han, F. Liao, Y. Zhang, X. Han, C. Xu, Ceramics International 45 (2019) 4059.
52. H. T. Zhu, J. Luo, J. K. Liang, G. H. Rao, J. B. Li, J. Y. Zhang, Z. M. Du, Physica B 403 (2008) 3141.
53. W. Wang, J Mater Sci: Mater. Electron 32 (12) (2021) 16662.
54. V. Narayanaswamy**,** I. A. Al-Omari, A. S. Kamzin, B. Issa, H. O. Tekin, H. Khourshid, H. Kumar, A. Mallya, S. Sambasivam, I. M. Obaidat, Nanomaterials 11 (2021) 1231. https://doi.org/10.3390/nano11051231]
55. P. R. Graves, C. Johnston, J. J. Campaniello, Mat. Res. Bull. 23 (1988) 1651.
56. S. B. Patil, H. S. Bhojya Naik, G. Nagaraju, Y. Shiralgi, Eur. Phys. J. Plus 133 (2018) 229. DOI 10.1140/epjp/i2018-12063-5.
57. J. Kreisel, G. Lucazeau, H. Vincent, J. Solid State Chem. 137 (1998) 127.
58. F. Naaz, H. K. Dubey, C. Kumari, P. Lahiri, SN Applied Sciences, 2 (2020) 808. https://doi.org/10.1007/s4, 2452-020-2611-9
59. O. N. Shebanova, P. Lazor, J. Solid State Chem. 174 (2003) 424.

60. P. Bera, R. V. Lakshmi, B. H. Prakash, K. Tiwari, A. Shukla, A. K. Kundu, K. Biswas, H. C. Barshilia, Phys. Chem. Chem. Phys. 22 (2020) 20087.
61. Z. Wang, R. T. Downs, V. Pischedda, R. Shetty, S. K. Saxena, C. S. Zha, Y. S. Zhao, D. Schiferl, A. Waskowska, Phys. Rev. B 68 (2003) 094101.
62. V. Bartunek, D. Sedmidubský, Š. Huber, M. Švecová, P. Ulbrich, O. Jankovský, Materials 11(7) (2018) 1241.
63. R. D. Shannon, Acta Cryst., A32, 751 (1976).
64. V. S. Shinde, V. Vinayak, S. P. Jadhav, N. D. Shinde, A. V. Humbe, K. M. Jadhav, J. Superconduct. Novel Magnetism 32 (4) (2019) 945.
65. S. M. Patange, S. E. Shirsath, K. S. Lohar, S. G. Algude, S. R. Kamble, N. Kulkarni, D. R. Mane, K. M. Jadhav, J. Magn. Magn. Mater. 325 (2013) 107.
66. L. Phor, S. Chahal, V. Kumar, J. Advanced Ceramics 9(5) (2020) 576.
67. T. R. Tatarchuk, M. Bououdina, N. D. Paliychuk, I. P. Yaremiy, V. V. Moklyak, J. Alloys Compd. 694 (2017) 777.
68. F. Gervais, B. Piriou, Phys. Rev. B 10 (1974) 1642.
69. F. Gervais, Mater. Sci. Eng. R 39 (2002) 29.
70. M. Bastianello, S. Gross, M. T. Elm, RSC Adv. 9 (2019) 33282.
71. H. D. Lutz, B. Müller, H. J. Steiner, J. Solid State Chem. 90 (1991) 54.
72. T. Shimada, T. Tachibana, T. Nakagawa, T. A. Yamamoto, J. Alloys Compd. 379 (2004) 122.
73. L. Degiorgi, I. Blatter-Morke, P. Wachter, Phys Rev B 35 (1987) 5421.
74. A. B. Kuzmenko, Review of Scientific Instruments 76 (8) (2005) 083108.
75. F. C. Jahoda, Phys. Rev. 107 (1957) 1261.
76. H. R. Phillip, E. A. Taft, Phys. Rev. 136 (1964) A1445.
77. K. Ramarao, B. Rajesh Babu, B. Kishore, V. Veeraiah, S. D. Ramarao, K. Rajasekhar and A. Venkateswara Rao, J. Electronic Materials 47(5) (2018) 2997.
78. R. Vishwarup, S. N. Mathad, Mat. Sci. Energy Techn. 3 (2020) 559.
79. S. A. Mazen, T. A. Elmosalami, International Scholarly Research Network ISRN Condensed. Matter. Physics (2011) 820726.
80. K. B. Modi, S. J. Shah, N. B. Pujara, T. K. Pathak, N. H. Vasoya, I. G. Jhala, J. Mol. Struct. 1049 (2013) 250.
81. T. R. Tatarchuk, N. D. Paliychuk, M. Bououdina, B. Al-Najar, M. Pacia, W. Macyk, A. Shyichuk, J. Alloys Compd. 731 (2018) 1256.
82. S. M. Patange, S. E. Shirsath, S. P. Jadhav, V. S. Hogade, S. R. Kamble, K. M. Jadhav, J. Mol. Struct. 1038 (2013) 40.

83. A. B. Rajput, S. Hazra, N. N. Ghosh, J. Experimental Nanoscience, 8(4) (2013) 629.
84. O. L. Anderson, J. Phys. Chem. Solid 24(7) (1963) 909.
85. N. Paunović, Z. Dohčević-Mitrović, D. M. Djokić, S. Aškrabić, S. Lazović, A. R. Abraham, B. Raneesh, N. Kalarikkale, S. Thomas, Materials Science in Semiconductor Processing 149 (2022) 106889.
86. A. R. Abraham, B. Raneesh, P. M. G. Nambissan, D. Sanyal, S. Thomas, N. Kalarikkal, Philosophical Magazine, Part A: Materials Science 100(1) (2020) 32. https://doi.org/10.1080/14786435.2019.1668576
87. L. V. Gasparov, D. B. Tanner, D. B. Romero, H. Berger, G. Margaritondo, L. Forro, Phys. Rev. B 62 (2000) 7939.
88. Z. Ž. Lazarević, A. N. Milutinović, Č. D. Jovalekić, V. N. Ivanovski, N. Daneu, I. Madjarević, N. Ž. Romčević, Mater. Res. Bull. 63 (2015) 239.
89. L.W. Finger, R. M. Hazen, A. M. Hofmeister, Phys. Chem. Minerals 13(4) (1986) 215.
90. P. Lichvár, M. Liška, D. Galušek, Ceramics – Silikáty 46(1) (2002) 25.
91. C. Murugesan, M. Perumal, G. Chandrasekaran, Physica B 448 (2014) 53.

Figure captions:

Fig. 1. a) X-ray diffractograms of cobalt ferrite samples obtained by various synthesis methods, arranged by rising unit cell parameter (*a*) from top to bottom; b) Dominant (311) Bragg reflection as an example of the shift of XRD reflections to lower angles with increasing lattice constant; c) Degree of the cation inversion (x) as a function of the lattice constant. Triangles are values obtained by Rietveld refinement and circles are values obtained by the structural analysis.

Fig. 2. Raman spectra of $CoFe_2O_4$ nanoparticle samples obtained by various methods of synthesis. From top to the bottom are spectra of the samples with ascending crystal constants. Raman spectra are deconvoluted in 7-8 Lorentzians and peaks are assigned as in normal cubic spinel. Peaks A_{1g} and $F_{2g}(1)$ are completely dissociated. The degree of the cation inversion, x_R, is estimated from the areas of $A_{1g}(1)$ and $A_{1g}(2)$ Lorentzians, see in the text.

Fig. 3. a) Raman spectra of ferrites $(M_{1-x}Fe_x)A[Fe_{2-x}M_x]B$, *M*=Mg, Fe, Co, Ni, Zn. The spectra of ferrites were deconvoluted so that could be more easily compared with the spectra of the investigated nano-powder of $CoFe_2O_4$. The modes related to the vibration of oxygen bonded to Fe in $FeFe_2O_4$ are indicated by a dotted line. b) Raman spectra of cobaltites MCo_2O_4, *M*=Mg, Fe, Co, Ni, Zn. The modes related to the vibration of oxygen bonded to Co^{3+} in $CoCo_2O_4$ are indicated by a dotted line. Arrows indicate "satellite" peaks. c) Cobalt spinel oxides CoB_2O_4, B^{3+}= Al, Fe, Co. d) Magnesium spinel oxides MgB_2O_4, B^{3+}= Al, Fe, Co.

Fig. 4. a) The dependence of wave numbers of Raman modes in ferrites MFe_2O_4, where *M* = Mg, Fe, Co, Ni, Zn, on the tetrahedral cation radius of M^{2+} cation; b) The dependence of wave numbers of Raman modes in ferrites on the effective radius of tetrahedral complex $M_{1-x}Fe_x$. In insert is the dependence of E_g mode on the radius of octahedral complex $Fe_{2-x}M_x$. c) The dependence of wave numbers of Raman modes in cobaltites MCo_2O_4, where *M* = Mg, Fe, Co, Ni, Zn, on the tetrahedral cation radius of M^{2+}.

Fig. 5. The degree of cation inversion for various $CoFe_2O_4$ samples estimated from Raman spectra and from XRD analysis as the function of lattice constant.

Fig. 6. Infrared reflectivity spectra of $CoFe_2O_4$ nanoparticles obtained by various synthesis procedures: Experimental spectra are presented by open circles and calculated spectra by solid lines. The best-fit parameters of simulated reflectivity spectra are given for each sample. At the bottom right is a graphic representation of the dependence of TO and LO oscillations on the degree of the cation inversion.

Fig. 7. Selected FIR Reflectivity spectra of $CoFe_2O_4$ nanoparticles fitted by DPP model with 10 phonon modes and a Drude therm. The fitting parameters for the main modes are listed first and the parameters of the additional modes are written in a smaller font after that.

Fig. 8. KK analysis of reflectivity spectra for two selected samples. Local maximums of $\varepsilon_2(\omega)$ correspond to the values of ω_{TO} for various sub-bands.

Fig. 9. Dependences of a) degree of invesion on stiffness and elastic constants and b) degree of inversion on Debye temperature.

Fig. 10. ATR-FTIR spectra of investigated $CoFe_2O_4$ nanoparticle samples obtained by various synthesis methods. On the left side is extended a part of the original spectra that correspond to the characteristic oscillations of cobalt ferrite. On the right side is full range of spectra with normalized intensity. Oscillations of the functional groups originating from atmospheric gases and water vapour absorbed on the sample surfaces are marked.

Fig. 11. a) Deconvolution of the ATR absorption spectra for samples US-CO and MC-CO in the range of “fingerprints”; b) The positions of deconvoluted modes for all samples as a function of cation inversion.

Table captions:

Table 1. Raman modes in the cobalt ferrite nanomaterials obtained by different synthesis methods. Mode A_{1g*} corresponds to maghemite.

Table 2. Force constants of IR modes in nanoparticle cobalt-ferrites; By ω_o is denoted the TO wave number of $F_{1u}(3)$ mode, ω_t is TO wave number of $F_{1u}(4)$ mode; M_A and M_B are effective masses of cations in A-tetrahedral and B-octahedral sites, respectively, calculated with cation inversion - x obtained by XRD. $k_{o,t(W)}$ are stretching force constants according to Waldron's model and $k_{o,t}$ force constants calculated directly.

Table 3. Stiffness constants* c_{11} ($c_{12} = 0.43 \cdot c_{11}$), elastic constants - bulk constant (B), Young's (E) and rigidity modulus (G), density of cobalt ferrite (ρ_{XRD}), sound velocities – longitudinal (V_l), transversal (V_s) and mean (V_m) and Debye temperature (Θ_D) obtained by elastic constant method. *Stiffness constant are calculated from the directly obtained force constants.

Table 4. Values of stiffness constants c_{11} and Debye temperatures for $CoFe_2O_4$ nanoparticle sample ("US-CO") and results for other ferrites estimated by elastic constants method and IR method (based on the data provided in the cited references). Characteristic wave numbers: ω_t, ω_o and ω_3, average force constant $k_{av} = (k_o + k_t)/2$, lattice constant a, necessary for calculation c_{11} and Θ_D are given, also. ρ_{XRD} (omitted for clarity) is calculated as $8M/(Na^3)$.

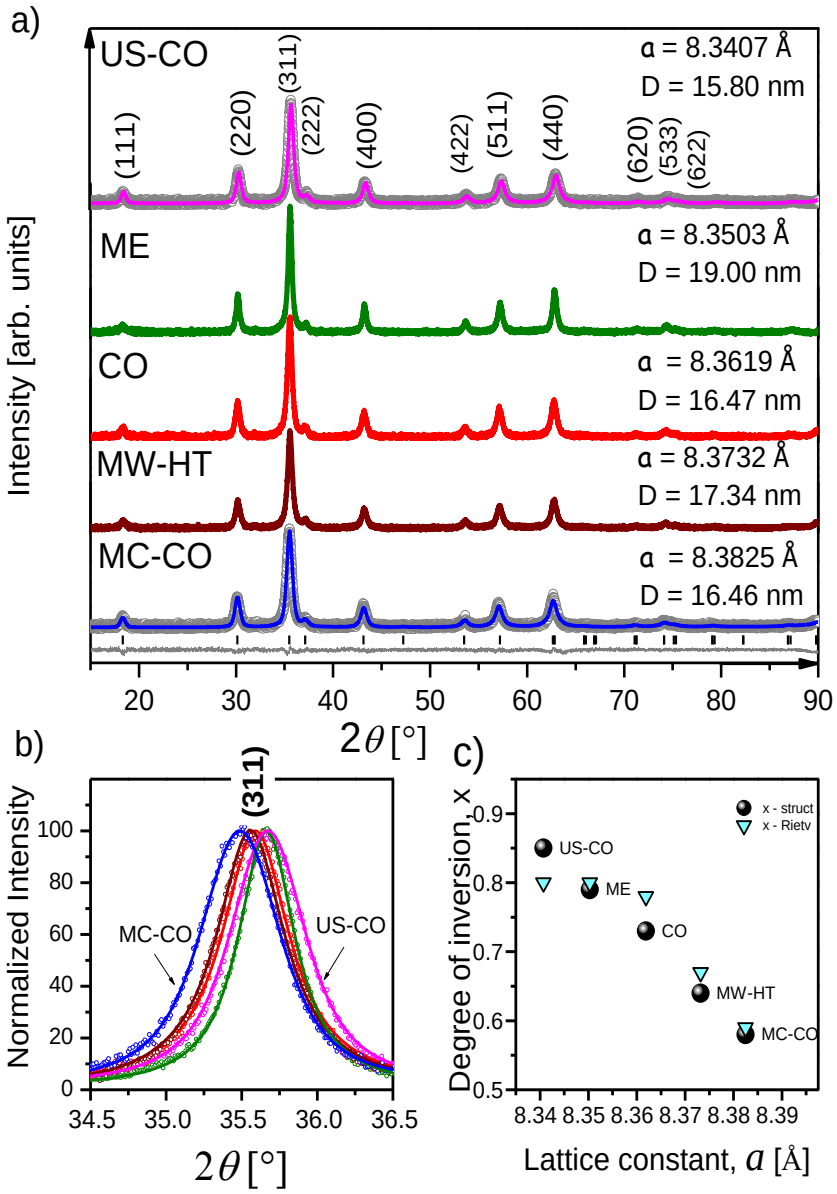
a)
US-CO
a = 8.3407 Å
D = 15.80 nm
(111)
(220)
(311)
(222)
(400)
(422)
(511)
(440)
(620)
(533)
(622)
ME
a = 8.3503 Å
D = 19.00 nm
CO
a = 8.3619 Å
D = 16.47 nm
MW-HT
a = 8.3732 Å
D = 17.34 nm
MC-CO
a = 8.3825 Å
D = 16.46 nm
Intensity [arb. units]
20
30
40
50
60
70
80
90
2θ [°]
b)
(311)
MC-CO
US-CO
Normalized Intensity
0
20
40
60
80
100
34.5
35.0
35.5
36.0
36.5
2θ [°]
c)
x - struct
x - Rietv
US-CO
ME
CO
MW-HT
MC-CO
Degree of inversion, x
0.5
0.6
0.7
0.8
0.9
8.34
8.35
8.36
8.37
8.38
8.39
Lattice constant, a [Å]

Figure 1

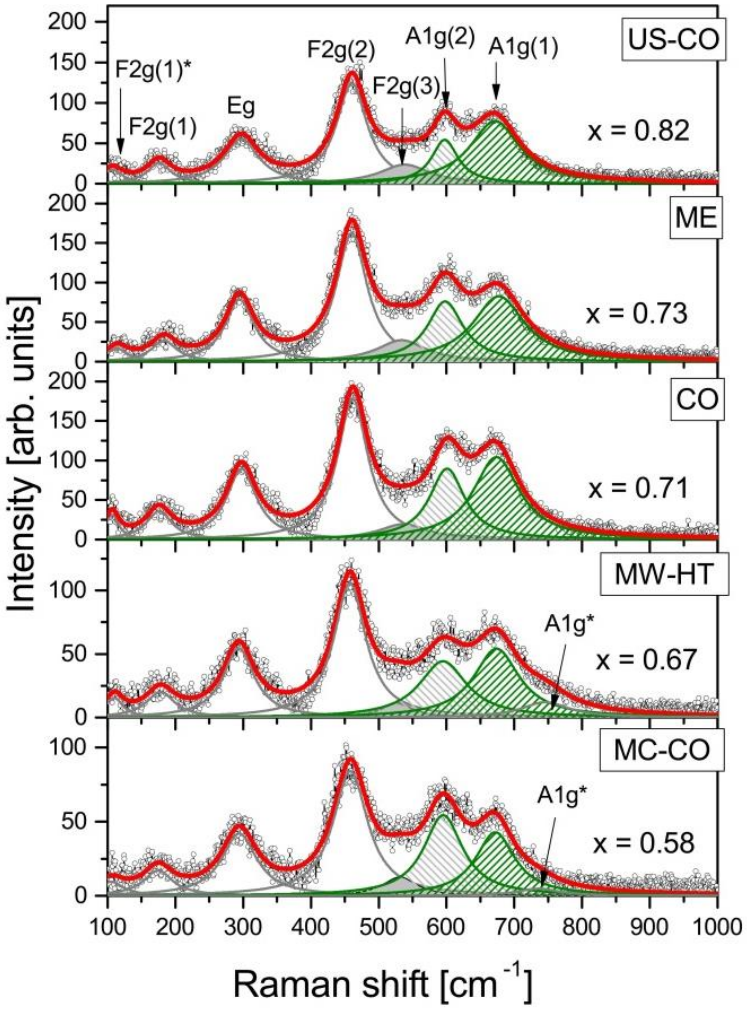
US-CO
ME
CO
MW-HT
MC-CO
x = 0.82
x = 0.73
x = 0.71
x = 0.67
x = 0.58
F2g(1)*
F2g(1)
Eg
F2g(2)
F2g(3)
A1g(2)
A1g(1)
A1g*
A1g*
Intensity [arb. units]
Raman shift [cm -1]

Figure 2

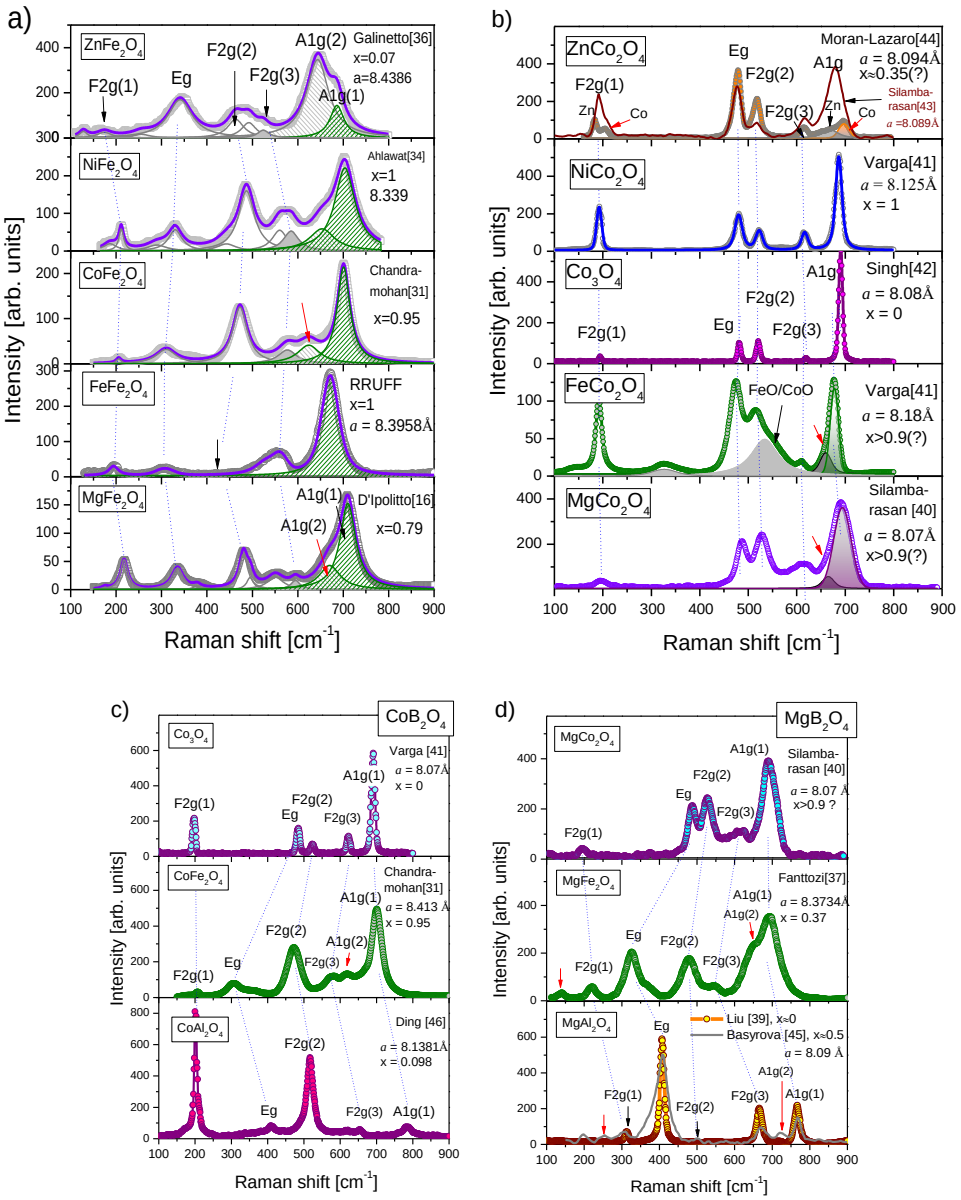
a)
ZnFe2O4
F2g(1)
Eg
F2g(2)
F2g(3)
A1g(2)
A1g(1)
Galinetto[36]
x=0.07
a=8.4386
NiFe2O4
Ahlawat[34]
x=1
8.339
CoFe2O4
Chandra-
mohan[31]
x=0.95
FeFe2O4
RRUFF
x=1
a = 8.3958Å
MgFe2O4
D'Ipolitto[16]
x=0.79
Intensity [arb. units]
Raman shift [cm-1]
b)
ZnCo2O4
Moran-Lazaro[44]
a = 8.094Å
x≈0.35(?)
Silamba-
rasan[43]
a =8.089Å
NiCo2O4
Varga[41]
a = 8.125Å
x = 1
Co3O4
A1g
Singh[42]
a = 8.08Å
x = 0
FeCo2O4
FeO/CoO
Varga[41]
a = 8.18Å
x>0.9(?)
MgCo2O4
Silamba-
rasan [40]
a = 8.07Å
x>0.9(?)
c)
CoB2O4
Varga [41]
a = 8.07Å
x = 0
CoFe2O4
Chandra-
mohan[31]
a = 8.413 Å
x = 0.95
CoAl2O4
Ding [46]
a = 8.1381Å
x = 0.098
d)
MgB2O4
MgCo2O4
Silamba-
rasan [40]
a = 8.07 Å
x>0.9 ?
MgFe2O4
Fanttozi[37]
a = 8.3734Å
x = 0.37
MgAl2O4
Liu [39], x≈0
Basyrova [45], x≈0.5
a = 8.09 Å

Figure 3

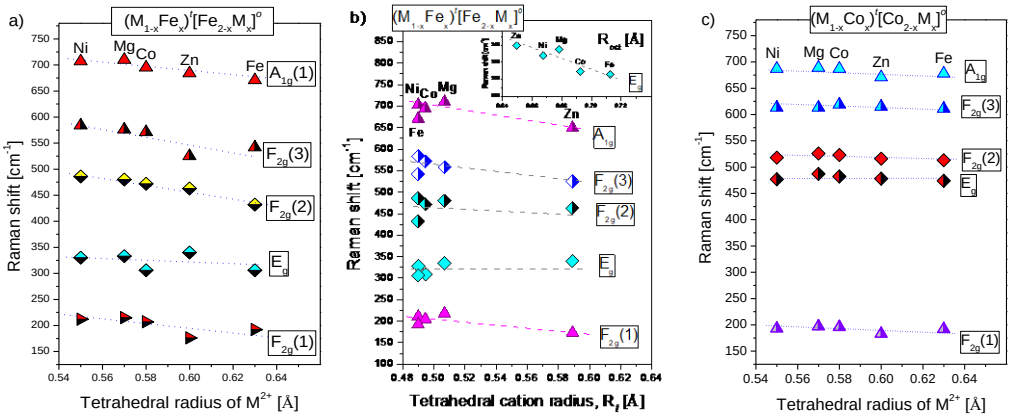
a)
$(M_{1-x}Fe_x)^t[Fe_{2-x}M_x]^o$
Ni
Mg
Co
Zn
Fe
$A_{1g}(1)$
$F_{2g}(3)$
$F_{2g}(2)$
E_g
$F_{2g}(1)$
Raman shift [cm^{-1}]
Tetrahedral radius of M^{2+} [Å]
b)
$(M_{1-x}Fe_x)^t[Fe_{2-x}M_x]^o$
R_{oct} [Å]
Ni
Co
Mg
Fe
Zn
A_{1g}
$F_{2g}(3)$
$F_{2g}(2)$
E_g
$F_{2g}(1)$
Raman shift [cm^{-1}]
Tetrahedral cation radius, R_t [Å]
c)
$(M_{1-x}Co_x)^t[Co_{2-x}M_x]^o$
Ni
Mg
Co
Zn
Fe
A_{1g}
$F_{2g}(3)$
$F_{2g}(2)$
E_g
$F_{2g}(1)$
Raman shift [cm^{-1}]
Tetrahedral radius of M^{2+} [Å]

Figure 4

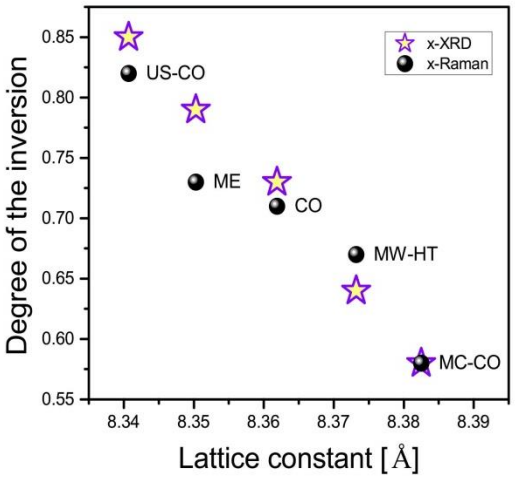
x-XRD
x-Raman
US-CO
ME
CO
MW-HT
MC-CO
Degree of the inversion
Lattice constant [Å]
0.85
0.80
0.75
0.70
0.65
0.60
0.55
8.34
8.35
8.36
8.37
8.38
8.39

Figure 5

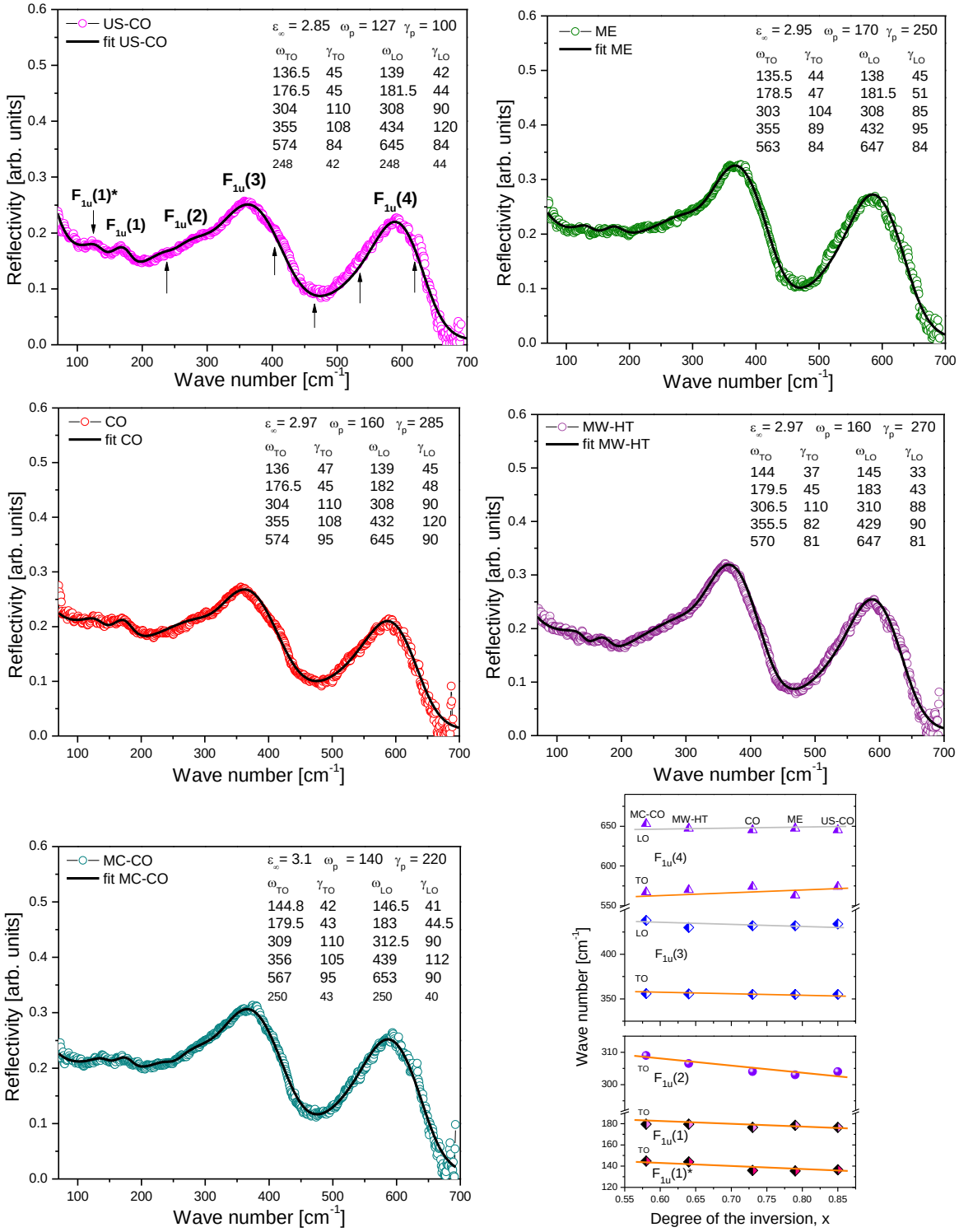
US-CO
fit US-CO
ε∞ = 2.85 ωp = 127 γp = 100
ωTO γTO ωLO γLO
136.5 45 139 42
176.5 45 181.5 44
304 110 308 90
355 108 434 120
574 84 645 84
248 42 248 44
F1u(1)*
F1u(1)
F1u(2)
F1u(3)
F1u(4)
ME
fit ME
ε∞ = 2.95 ωp = 170 γp = 250
ωTO γTO ωLO γLO
135.5 44 138 45
178.5 47 181.5 51
303 104 308 85
355 89 432 95
563 84 647 84
CO
fit CO
ε∞ = 2.97 ωp = 160 γp = 285
ωTO γTO ωLO γLO
136 47 139 45
176.5 45 182 48
304 110 308 90
355 108 432 120
574 95 645 90
MW-HT
fit MW-HT
ε∞ = 2.97 ωp = 160 γp = 270
ωTO γTO ωLO γLO
144 37 145 33
179.5 45 183 43
306.5 110 310 88
355.5 82 429 90
570 81 647 81
MC-CO
fit MC-CO
ε∞ = 3.1 ωp = 140 γp = 220
ωTO γTO ωLO γLO
144.8 42 146.5 41
179.5 43 183 44.5
309 110 312.5 90
356 105 439 112
567 95 653 90
250 43 250 40
Reflectivity [arb. units]
Wave number [cm-1]
MC-CO MW-HT CO ME US-CO
LO
TO
F1u(4)
F1u(3)
F1u(2)
F1u(1)
F1u(1)*
Wave number [cm-1]
Degree of the inversion, x

Figure 6

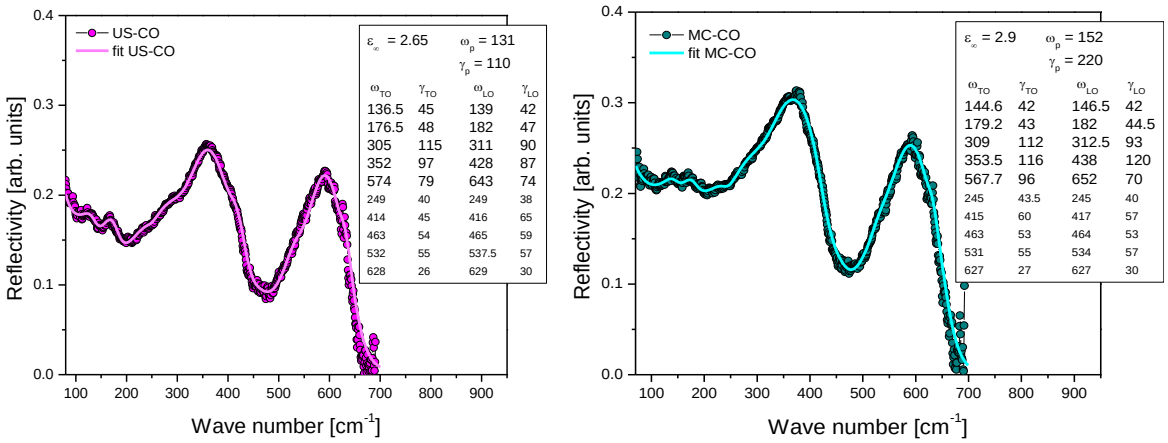
US-CO
fit US-CO
ε∞ = 2.65
ωp = 131
γp = 110
ωTO γTO ωLO γLO
136.5 45 139 42
176.5 48 182 47
305 115 311 90
352 97 428 87
574 79 643 74
249 40 249 38
414 45 416 65
463 54 465 59
532 55 537.5 57
628 26 629 30
Reflectivity [arb. units]
Wave number [cm-1]
MC-CO
fit MC-CO
ε∞ = 2.9
ωp = 152
γp = 220
ωTO γTO ωLO γLO
144.6 42 146.5 42
179.2 43 182 44.5
309 112 312.5 93
353.5 116 438 120
567.7 96 652 70
245 43.5 245 40
415 60 417 57
463 53 464 53
531 55 534 57
627 27 627 30
Reflectivity [arb. units]
Wave number [cm-1]

Figure 7

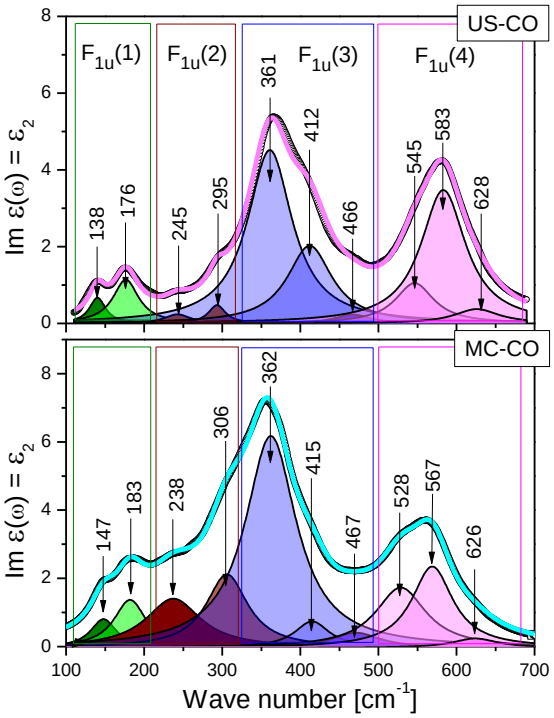
US-CO
MC-CO
F1u(1)
F1u(2)
F1u(3)
F1u(4)
Im ε(ω) = ε2
Wave number [cm-1]
138
176
245
295
361
412
466
545
583
628
147
183
238
306
362
415
467
528
567
626

Figure 8

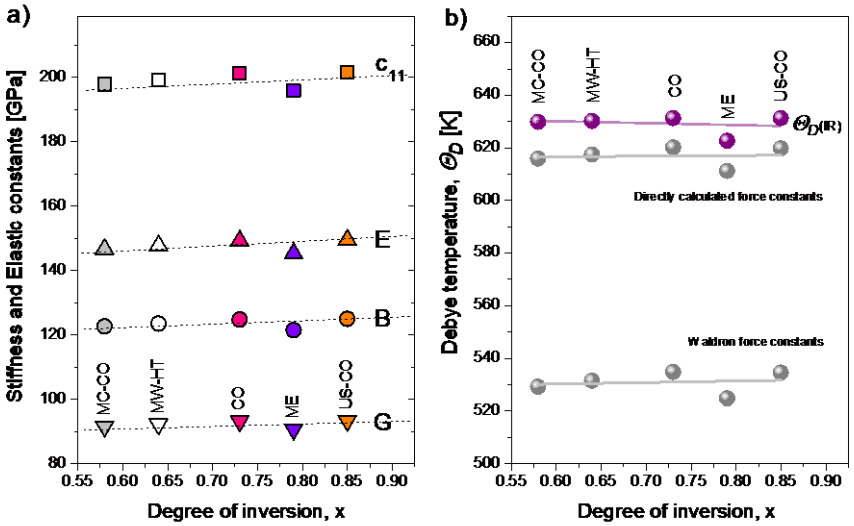
a)
Stiffness and Elastic constants [GPa]
c11
E
B
G
MC-CO
MW-HT
ME
US-CO
Degree of inversion, x
b)
Debye temperature, ΘD [K]
ΘD(IR)
Directly calculated force constants
Waldron force constants
Degree of inversion, x

Figure 9

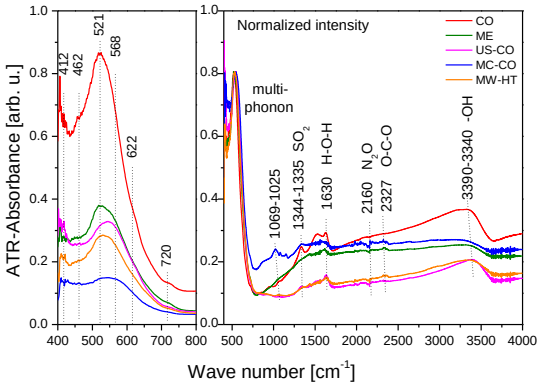
ATR-Absorbance [arb. u.]
Wave number [cm-1]
Normalized intensity
CO
ME
US-CO
MC-CO
MW-HT
multi-
phonon
412
462
521
568
622
720
1069-1025
1344-1335
SO2
H-O-H
1630
2160
N2O
O-C-O
2327
3390-3340
-OH

Figure 10

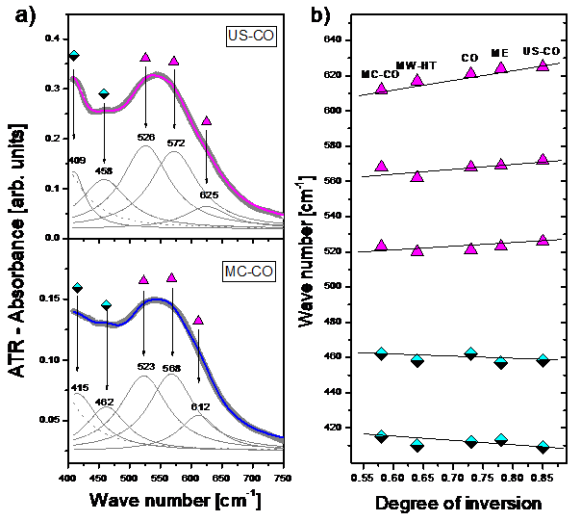
a)
US-CO
409
458
526
572
625
MC-CO
415
462
523
568
612
ATR - Absorbance [arb. units]
Wave number [cm-1]
b)
MC-CO
MW-HT
CO
ME
US-CO
Wave number [cm-1]
Degree of inversion

Figure 11

Table 1. Raman modes in the cobalt ferrite nanomaterials obtained by different synthesis methods. Mode A_{1g^*} corresponds to maghemite.

Mode [cm^{-1}]	US-CO	ME	CO	MW-HT	MC-CO
$F_{2g}(1)$*	102	113	104	110	105
$F_{2g}(1)$	175	183	176	177	174
E_g	297	295	297	293	294
$F_{2g}(2)$	460	460	462	457	458
$F_{2g}(3)$	539	533	536	526	531
$A_{1g}(2)$	597	598	601	595	595
$A_{1g}(1)$	671	677	675	674	672
A_{1g}*	-	-	-	746	738

Table 2. Force constants of IR modes in nanoparticle cobalt-ferrites; By ω_o is denoted the TO wave number of $F_{1u}(3)$ mode, ω_t is TO wave number of $F_{1u}(4)$ mode; M_A and M_B are effective masses of cations in A-tetrahedral and B-octahedral sites, respectively, calculated with cation inversion - x obtained by XRD. $k_{o,t(W)}$ are stretching force constants according to Waldron's model and $k_{o,t}$ force constants calculated directly.

Sample	x	M_A	M_B	ω_o [cm^{-1}]	ω_t [cm^{-1}]	$k_{o(W)}$ [Nm^{-1}]	$k_{t(W)}$ [Nm^{-1}]	k_o [Nm^{-1}]	k_t [Nm^{-1}]
US-CO	0.85	56.265	57.118	355	574	76.50	173.59	93.24	242.97
ME	0.79	56.451	57.024	355	563	76.46	164.73	93.21	233.92
CO	0.73	56.637	56.932	355	574	76.41	173.88	93.18	243.32
MW-HT	0.64	56.916	56.792	355.5	570	76.56	170.62	93.39	240.20
MC-CO	0.58	57.102	56.699	356	567	76.73	168.11	93.62	237.85

Table 3. Stiffness constants* c_{11} (c_{12} = 0.43·c_{11}), elastic constants - bulk constant (B), Young's (E) and rigidity modulus (G), density of cobalt ferrite (ρ_{XRD}), sound velocities – longitudinal (V_l), transversal (V_s) and mean (V_m) and Debye temperature (Θ_D) obtained by elastic constant method. *Stiffness constant are calculated from the directly obtained force constants.

Sample (x)	c_{11} [GPa]	B [GPa]	E [GPa]	G [GPa]	ρ_{XRD} [kg m^{-3}]	V_l [m s^{-1}]	V_t [m s^{-1}]	V_m [m s^{-1}]	Θ_D [K]
US-CO (0.85)	201.52	124.94	149.41	93.38	5373	6124	4169	4545	619.77
ME (0.79)	195.88	121.45	145.23	90.76	5367	6041	4112	4483	611.14
CO (0.73)	201.21	124.75	149.18	93.24	5331	6143	4182	4559	620.10
MW-HT (0.64)	199.20	123.50	147.69	92.31	5309	6125	4170	4546	617.42
MC-CO (0.58)	197.72	122.58	146.59	91.62	5272	6124	4169	4545	615.83

Table 4. Values of stiffness constants c_{11} and Debye temperatures for $CoFe_2O_4$ nanoparticle sample ("US-CO") and results for other ferrites estimated by elastic constants method and IR method (based on the data provided in the cited references). Characteristic wave numbers: ω_t, ω_o and ω_3, average force constant $k_{av} = (k_o + k_t)/2$, lattice constant a, necessary for calculation c_{11} and Θ_D are given, also. ρ_{XRD} (omitted for clarity) is calculated as $8M/(Na^3)$.

Ferrite	ω_t [cm^{-1}]	ω_o [cm^{-1}]	ω_3 [cm^{-1}]	k_{av} [N m^{-1}]	a [Å]	c_{11} [GPa]	Θ_D [K]	$\Theta_{D(IR)}$ [K]
$CoFe_2O_4$ (US-CO)	574	355	304	168.11	8.3407	201.5	619.8	631.3
$NiFe_2O_4$ [26]	557	399	328	173.14	8.3368	207.7	629.1	636.3
$NiFe_2O_4$ [72]	565.6	377	339.4	170.37	8.458	201.4	624.1	650.7
$MgFe_2O_4$ [85] [86]	542	436	332	171.74	8.376	205.1	643.4	628.4
Fe_3O_4 [87]	560	350	250	160.53	?			582.4
Fe_3O_4 [20]	570	370	237*	169.99	8.3554[#]	203.4	624.7	580.2
$ZnFe_2O_4$ [72]	529.3	360.5	340.8	154.43	8.4585	182.6	591.4	625.6
$ZnFe_2O_4$ [88]	550	380	307	167.23	8.4020	198.6	615.4	616.2